NASA-CR-191073

NAG3-1172

H_2 ARCJET PERFORMANCE MAPPING PROGRAM

IN-20
145798
P, 51

Subcontract 90-1314/7293

FINAL REPORT

92-R-1615

Prepared for:

Texas Tech. University/NASA LeRC/SDIO

Submitted by:

Rocket Research Company
Olin Aerospace Division
11441 Willows Road N.E.
Redmond, WA 98073-9709

January 31, 1992

ROCKET RESEARCH COMPANY

REDMOND, WASHINGTON — Olin AEROSPACE DIVISION

H_2 ARCJET PERFORMANCE MAPPING PROGRAM

Subcontract 90-1314/7293

FINAL REPORT

92-R-1615

Prepared for:

Texas Tech. University/NASA LeRC/SDIO

Submitted by:

Rocket Research Company
Olin Aerospace Division
11441 Willows Road N.E.
Redmond, WA 98073-9709

January 31, 1992

DOCUMENT REVISION RECORD
DOCUMENT NO. 92-R-1615

REVISION AND DATE	DESCRIPTION OF CHANGE/ REVISION AND PAGES AFFECTED	EFFECTIVITY
Orig. 1/31/92		SY 2/4/92

TABLE OF CONTENTS

LIST OF FIGURES

LIST OF TABLES

FINAL REPORT

H_2 ARCJET PERFORMANCE MAPPING PROGRAM

Subcontract 90-1314/7293

SDIO/NASA/Texas Tech.

1.0 Introduction/Summary

This is the final report for subcontract 90-1314/7294 prepared for Texas Tech. University by Rocket Research Company. This work was performed during the period of March, 1991 to January, 1992.

High power H_2 arcjets are being considered for electric powered orbit transfer vehicles (EOTV). Mission analyses indicate that the overall arcjet thrust efficiency is very important since increasing the efficiency increases the thrust, and thereby reduces the total trip time for the same power. For example, increasing the thrust efficiency at the same specific impulse from 30% to 40% will reduce the trip time by 25%. For a 200 day mission, this equates to 50 days, which results in lower ground costs and less time during which the payload is dormant. Arcjet performance levels of 1200 seconds specific impulse (Isp) at 35% to 40% efficiency with lifetimes of over 1000 hours are needed to support EOTV missions.

The power level targeted for the present work was 10-15 kW. Such a thruster can be used to support EOTV's having power levels from 20 kW and higher by firing several thrusters simultaneously. Although higher efficiencies are generally obtained at higher powers, it was thought that this power level provided an appropriate balance between efficiency and near term mission suitability.

Little work has been done recently to optimize the H_2 arcjet performance. Work done in the 1960's by the Giannini Corporation focused on a unique arcjet configuration wherein the arc attaches in a subsonic region upstream of the throat, and which used regenerative cooling passages to improve the efficiency. This configuration is shown in Figure 1-1. Very high efficiencies were quoted for this configuration, and a 500 hour lifetest was completed at 1000

GIANNINI ARCJET CONCEPT

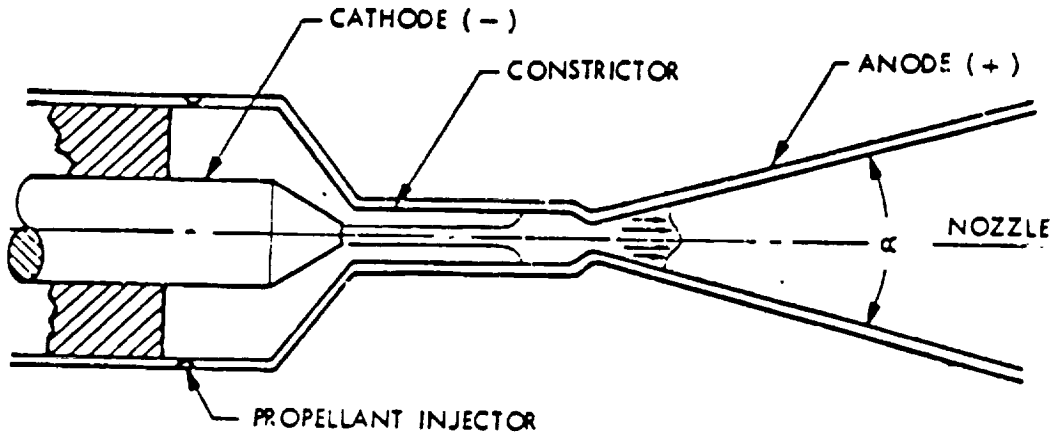

Figure 1-1

seconds I_{sp} and 55% efficiency at 30 kW input power. In theory, this configuration reduces the frozen flow losses by increasing the recombination in the subsonic constrictor. The regenerative passages both cool the constrictor region and pre-heat the incoming propellant. These high efficiency levels were not achieved during tests conducted at AVCO during the same period, nor has NASA or RRC come close with recent conventional arcjet tests.

Because of the potential to achieve very high efficiency levels, the objective of this program was to evaluate the ability of a scaled Giannini-style thruster to achieve the performance levels quoted in the previous literature while operating at a reduced nominal power of 10 kW. To meet this objective, a review of the past literature was conducted, scaling relationships were developed and applied to establish critical dimensions, a development thruster was designed with the aid of the plasma analysis model KARNAC and finite element thermal modelling, test hardware was fabricated, and a series of performance tests were conducted in RRC's Cell 11 vacuum chamber with its null-balance thrust stand.

The results obtained with the single configuration tested are encouraging. The thruster operated very stably over a power range of from 4 kW to 12 kW. There was virtually no erosion seen after approximately 20 hours of operation. Performance values were very repeatable. The efficiency levels obtained up to about 950 seconds I_{sp} were significantly higher than for conventional designs. Above that I_{sp} level, the efficiency was lower. These trends are shown in Figure 1-2 for 10 kW thruster power, along with RRC IRAD and NASA conventional data.

Although the initial results fall short of reproducing Giannini's reported performance levels, it is recommended that further investigations of this novel arcjet concept be conducted. Body temperature measurements and estimates of the effectiveness of the regenerative passages suggest that the efficiencies could be improved by reducing the thermal losses to the long subsonic constrictor. As will be discussed in more detail in the rest of the report, it appears that the constrictor was sized too large for this power level. Modifications to increase the temperature of the constrictor region are also recommended. Specific design recommendations are presented in section 7.0 Conclusions/Recommendations.

Isp Versus Efficiency

Hydrogen Propellant, 10kW

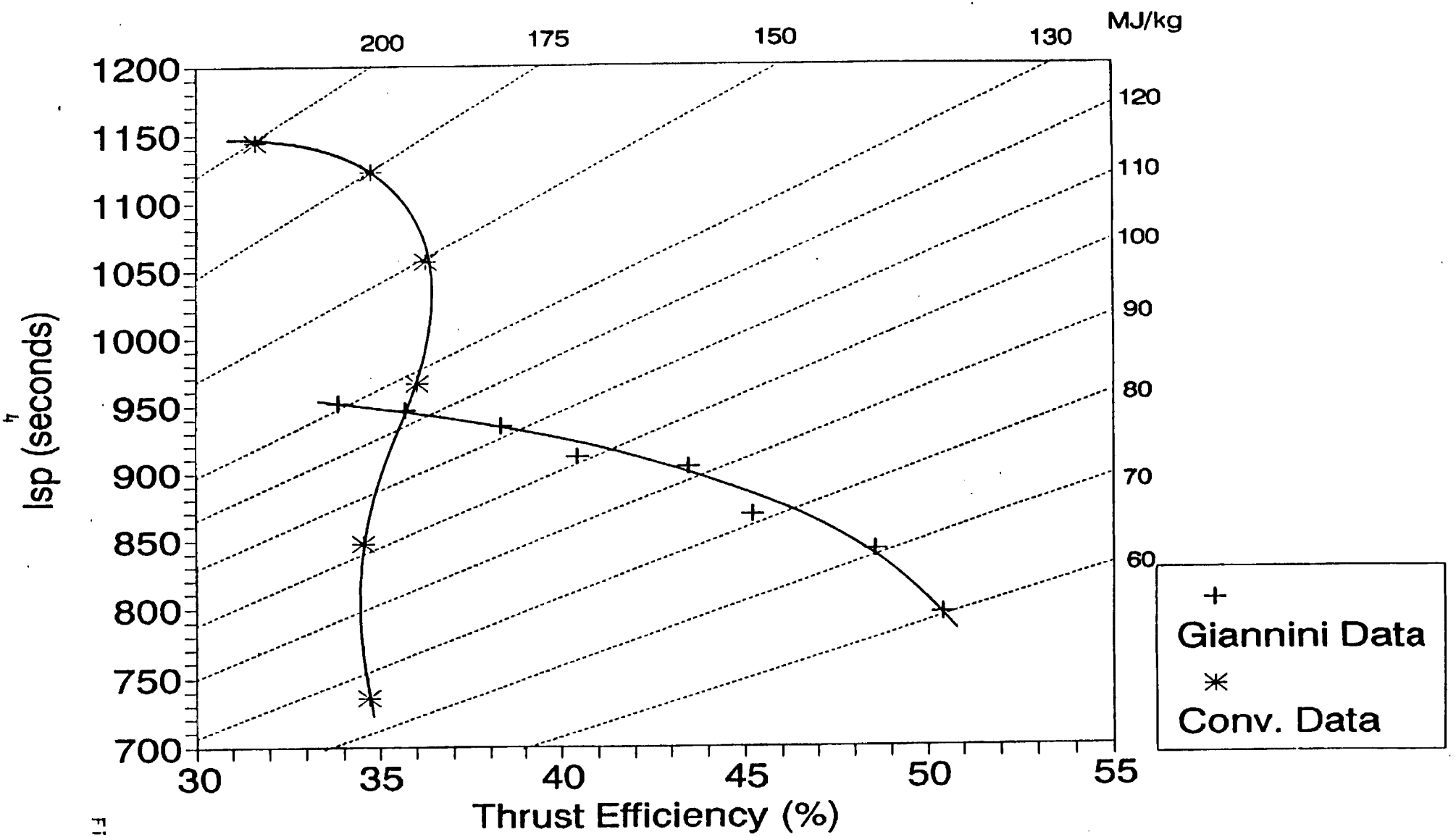

Figure 1-2

2.0 Review of Past Work

A review of the literature on the Giannini thruster shown in Figure 2-1 was completed. [1,2,3] Several observations were made:

1. The thrust efficiencies reported for the radiation cooled design are 10 to 15 percentage points higher than for the AVCO R-2 design in the 1000 second specific impulse range, but drop below the AVCO data above 1200 seconds, as shown in Figure 2-2.

2. The regenerative design increases the efficiency by approximately 10 percentage points (to 55% nominal) at around 1000 seconds. This compares with 42% for the AVCO design. Higher specific impulse values could not be obtained with this configuration due to high thermal loads on the electrodes.

3. Operating voltages were very high, typically in the 200 to 250 V range, for the regenerative design.

4. The thermal design was very critical. Numerous mechanical difficulties were experienced with the regenerative design.

3.0 Design/Analysis Summary

A scaling exercise was conducted to produce a 10 kW design. There are four parameters that were used. These are: power/flow rate ($P/\dot{m}$-specific energy); power/throat area (P/A^*-power flux); inlet pressure (p_{in}); and the heat flux to the constrictor surfaces (Q_s/constrictor area). At constant thrust efficiency, $P/\dot{m}$ is proportional to I_{sp}^2. The inlet pressure affects the wall heat transfer and the chemical kinetic rates. Chemistry rates for ionization and dissociation by two body collisional processes are proportional to p^2, while the reverse reactions are three body processes proportional to p^3. Maintaining the same inlet pressure during scaling should keep the pressure profile similar, and hence the heat flux and chemistry rates should also be similar.

GIANNINI THRUSTER

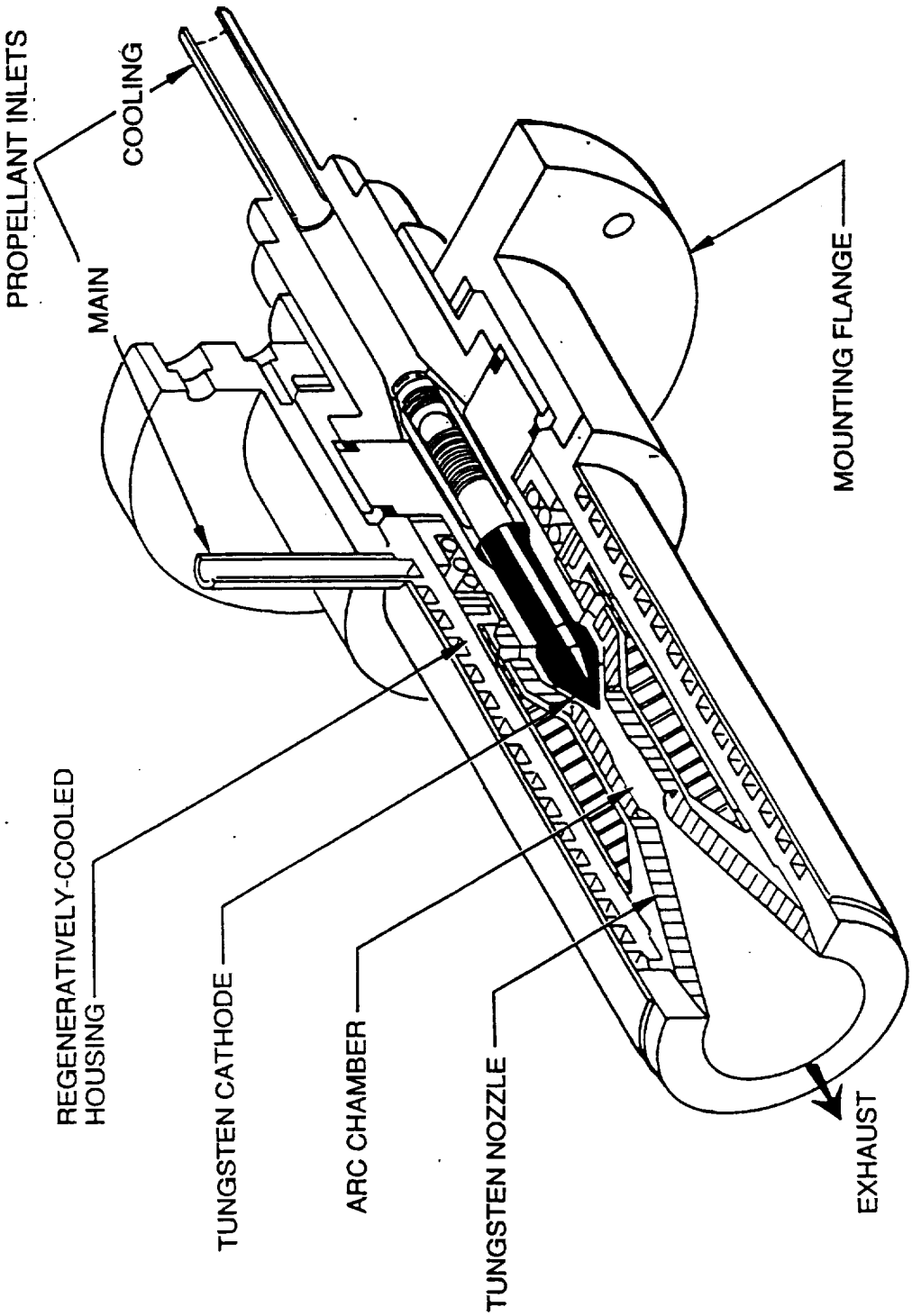

Figure 2-1

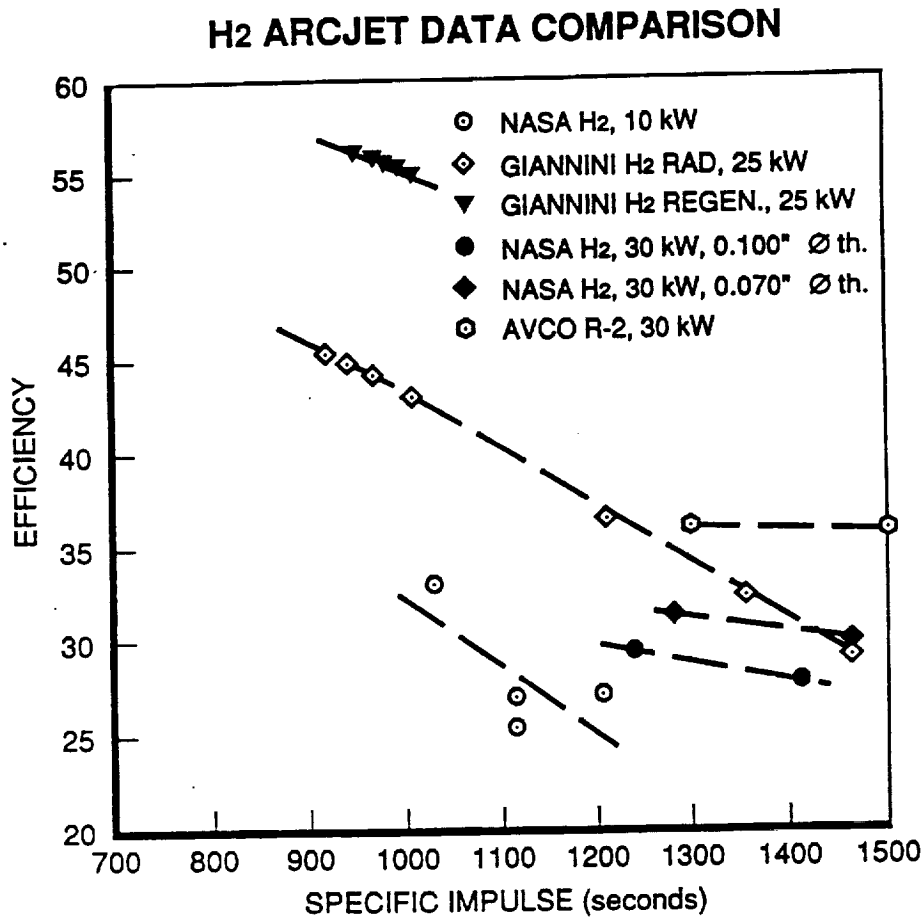
H2 ARCJET DATA COMPARISON
NASA H2, 10 kW
GIANNINI H2 RAD, 25 kW
GIANNINI H2 REGEN., 25 kW
NASA H2, 30 kW, 0.100" Ø th.
NASA H2, 30 kW, 0.070" Ø th.
AVCO R-2, 30 kW
EFFICIENCY
60
55
50
45
40
35
30
25
20
700
800
900
1000
1100
1200
1300
1400
1500
SPECIFIC IMPULSE (seconds)

Figure 2-2

The throat and inlet pressures can be related to the heat added in the subsonic region of choked flow. The throat pressure can be estimated as:

$$p^* = \frac{1}{A^* k^*} \frac{1}{\sqrt{k^* + \frac{1}{2}}} \sqrt{\dot{m} P}$$

To scale with constant p^* and constant $P/\dot{m}$ results in constant P/A^*. Heat flux considerations suggest that the lengths be scaled with radii. The results of these scaling methods are summarized in Figure 3-1.

An analysis was conducted using RRC's KARNAC code to calculate the energy flux to the constrictor walls and the current distribution. The results are shown in Figure 3-2. There is a very concentrated heat flux at the upstream corner of the constrictor. This is due primarily to the radiation from the high ohmic heating zone just off the cathode tip. There is another high energy flux region at the throat, as might be expected. This profile was incorporated into the thruster thermal model.

The current flux distribution shows most of the current being distributed along the slightly expanded region of the constrictor just before the throat. This supports the assumption that most of the heat addition is occurring in the subsonic region.

The thruster design is shown in Figure 3-3. The diameter of the anode is 2.0". Conax-style ram seals are used to seal the thruster around the cathode. The anode consists of two parts, which was necessary to create the stepped subsonic constrictor. One part includes the nozzle, throat, and part of the constrictor. It is lapped and press fit into a molybdenum body. The other part includes the injector holes and the upstream part of the constrictor. The joint between the two anode halves is lapped. The regenerative passage is created by forcing the gas down the outside of an annular baffle which is held in place between the injector and the cathode insulator. The gas returns along the outside wall of the constrictor, and then passes through the injector. The insulator parts are held in place by Belville washers which are trapped between the insulator tube and part of the Conax seal assembly.

The molybdenum anode body is attached to the main arcjet body by means of a large nut. Split rings are placed around the anode body after the nut is slipped over the upstream end. A graphoil seal is used between the two bodies. The tolerances around the seal are very tight to

GIANNINI SCALING

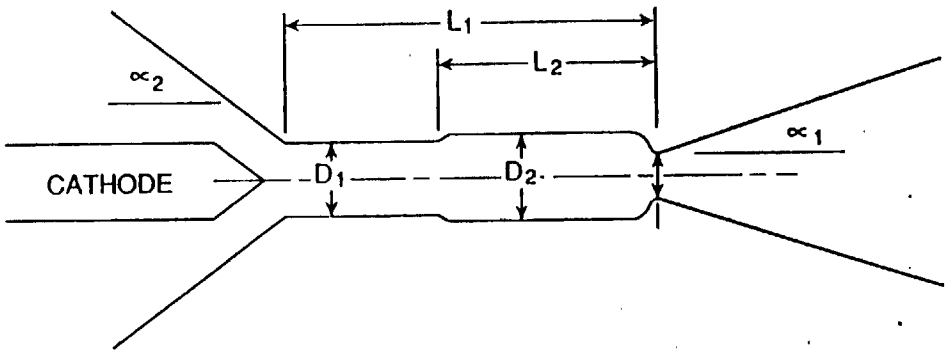

Parameter	Principle Effect	Scaling Rational	30 kW	10 kW
$P/\dot{m}$	I_{sp}^2 and enthalpy	Keep I_{sp} = 1,000 seconds	0.25 gm/sec	0.083 gm/sec
D_3	Controls choking point and subsonic heat addition	Keep p* = const. ⇨ P/D_3^2 = const.	0.475 cm	0.274 cm
D_1	Velocity in subsonic section	D_1/D_3 = const.	0.635 cm	0.367 cm
L_1	Area of constrictor	Keep heat flux similar L_1/D_1 = const.	3.18 cm	1.83 cm
D_2	Control current attachment	D_2/D_1 = const.	0.699 cm	0.403
L_2	Control current attachment	$L_1/L_2 = 2$	1.59 cm	0.915 cm
α_1	Mack acceleration and recombination in nozzle	Adjust with h* or I_{sp}^2 or $P/\dot{m}$	30°	30°
α_2	Arc startup and stability	Past experience	45°	30°

Figure 3-1

ANALYSIS RESULTS – GIANNINI STYLE THRUSTER

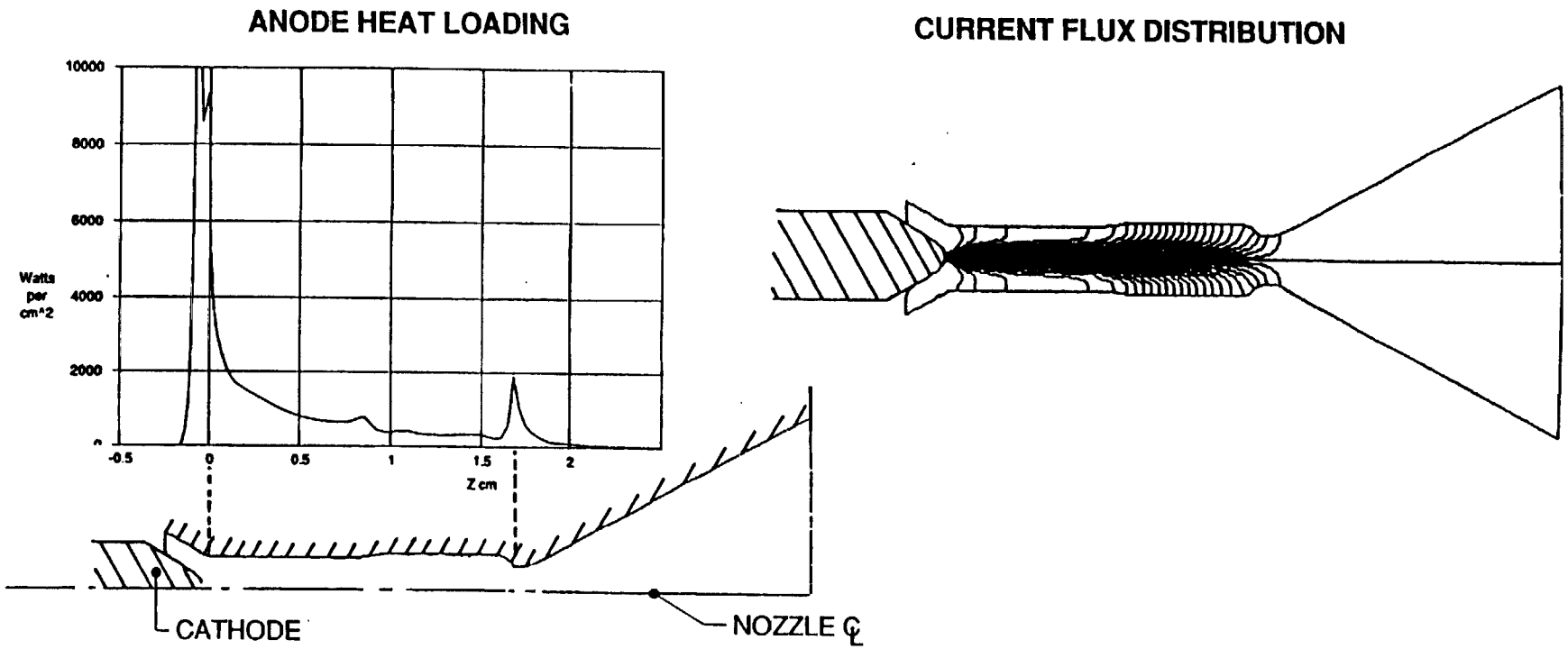

Figure 3-2

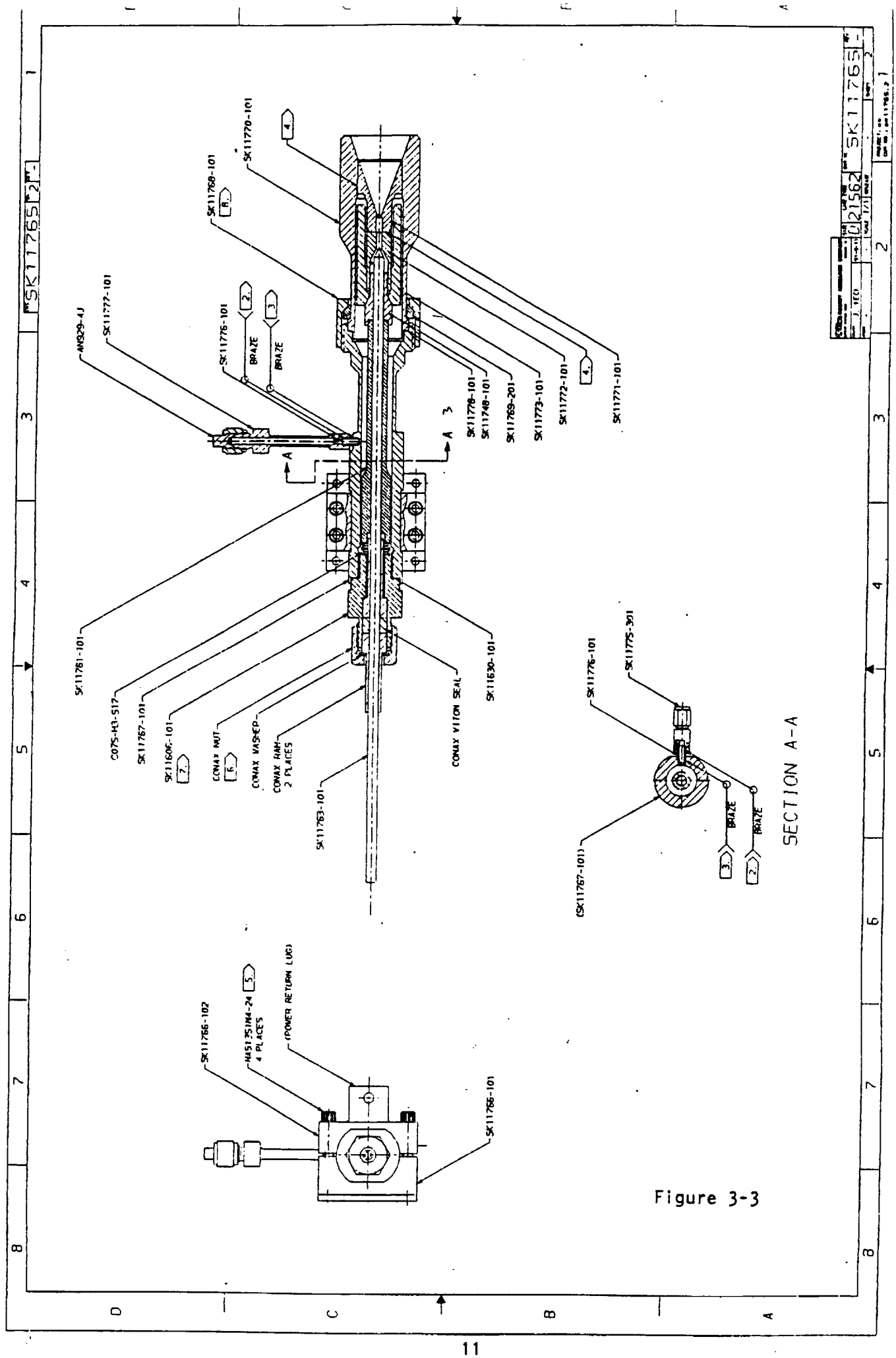
SK11765
SK11770-101
SK11768-101
SK11772-101
AN929-4J
SK11776-101
BRAZE
BRAZE
SK11778-101
SK11748-101
SK11769-201
SK11773-101
SK11772-101
SK11771-101
SK11781-101
C075-M3-517
SK11767-101
SK11606-101
CONAX NUT
CONAX WASHER
CONAX WAM 2 PLACES
SK11763-101
CONAX VITON SEAL
SK11630-101
SK11776-101
SK11775-301
(SK11767-101)
BRAZE
BRAZE
SECTION A-A
SK11766-102
MS51351N4-24 4 PLACES
(POWER RETURN LUG)
SK11766-101

Figure 3-3

minimize the exposure of the grapholl to the H_2 to prevent degradation of the seal. The position of this seal was determined on the basis of thermal model predictions to maintain the temperature below 1100°F. RRC's past experience indicated that the graphoil seal would not degrade at these temperatures when exposed to H_2. An anti-seize compound is used to prevent the threads from galling. The propellant feed line is brazed into the side of the molybdenum arcjet body.

This thruster proved to be easy to assemble, and allowed for disassembly and reassembly while mounted on the thrust stand. No leaks occurred during any of the testing. The thruster is shown in Figures 3-4 and 3-5.

Originally a non-regenerative design was also created, as shown in Figure 3-6. This uses most of the same parts, with the exception of the two anode halves. The intent was to determine through testing the impact of the regenerative heating of the propellant. Unfortunately, funding limitations prevented this configuration from being built and tested.

Thermal modelling was performed to predict temperatures in key areas. The finite element model is shown in Figure 3-7. Several iterations were made before the final design was selected. The input conditions were an H_2 flow rate of 115 mg/sec, and a power distribution on the anode as predicted by the KARNAC analysis discussed above. The total power deposited along the constrictor walls was about 3200 W. Conduction and radiation to ambient temperature surroundings were assumed.

Originally, the gas was allowed to enter into an annular plenum area before passing through the injector holes. The model predicted that the gas was cooled significantly in this plenum, so it was eliminated.

Initial constrictor temperatures were excessive, so the anode nozzle wall thickness was increased to conduct more heat to the outer body.

An assessment was done of the effectiveness of the heat exchanger passage. The contact surface area was arbitrarily increased by a factor of two. This had little effect on the predicted gas temperature, so it was decided to not add any tortuous paths (e.g, a helical flow path) to the heat exchanger.

ORIGINAL PAGE
BLACK AND WHITE PHOTOGRAPH

ARCJET ASSEMBLY

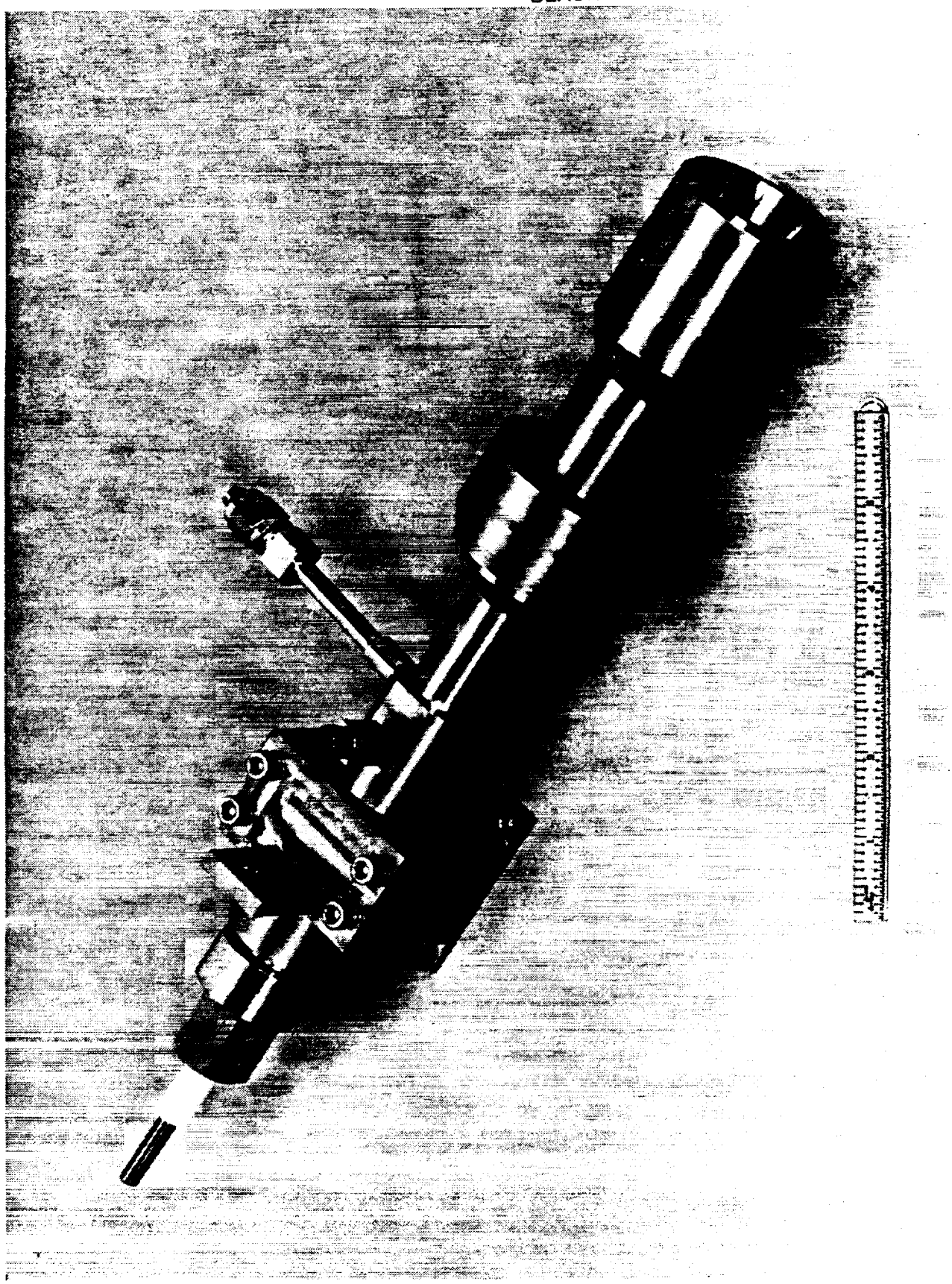

Figure 3-4

ORIGINAL PAGE
BLACK AND WHITE PHOTOGRAPH

ARCJET PIECE PARTS

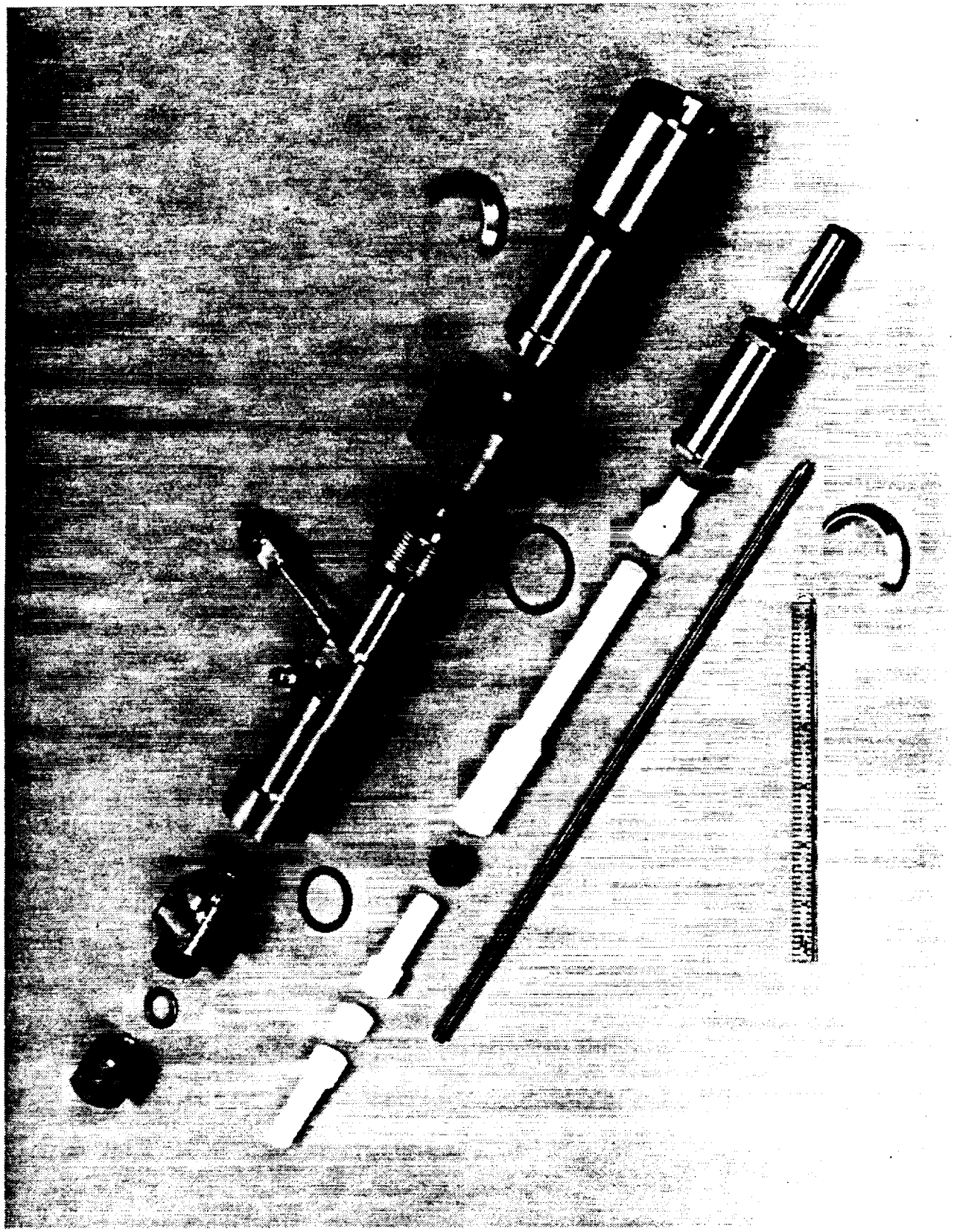

Figure 3-5

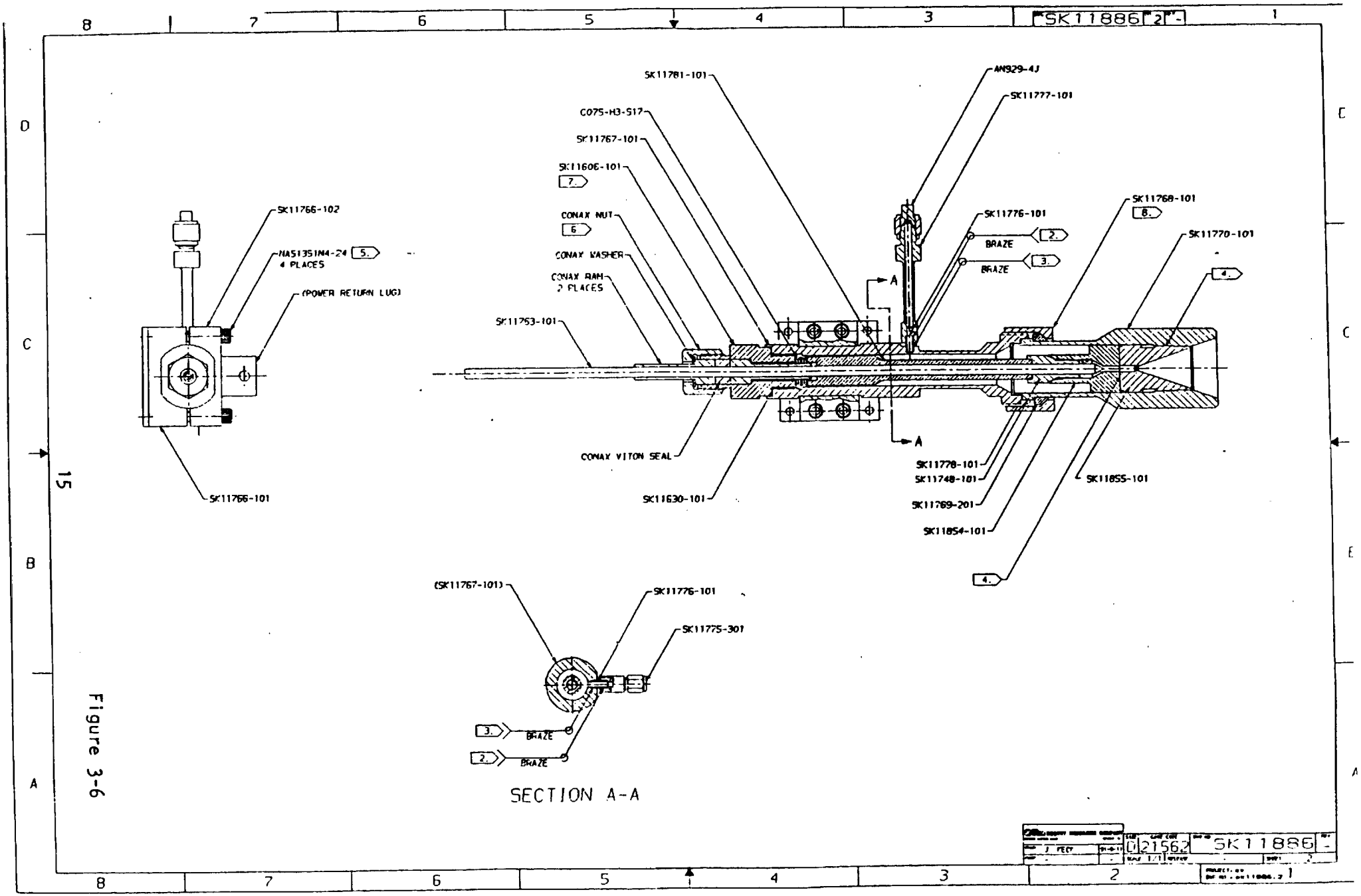
SK11766-102
NAS1351N4-24 5.
4 PLACES
(POWER RETURN LUG)
SK11766-101
SK11781-101
C075-H3-S17
SK11767-101
SK11606-101
7.
CONAX NUT
6
CONAX WASHER
CONAX RAM
2 PLACES
SK11753-101
CONAX VITON SEAL
SK11630-101
AN929-4J
SK11777-101
SK11776-101
BRAZE 2.
BRAZE 3.
SK11768-101
8.
SK11770-101
4.
A
A
SK11778-101
SK11748-101
SK11769-201
SK11854-101
SK11855-101
4.
(SK11767-101)
SK11776-101
SK11775-301
3.
BRAZE
2.
BRAZE
SECTION A-A

Figure 3-6

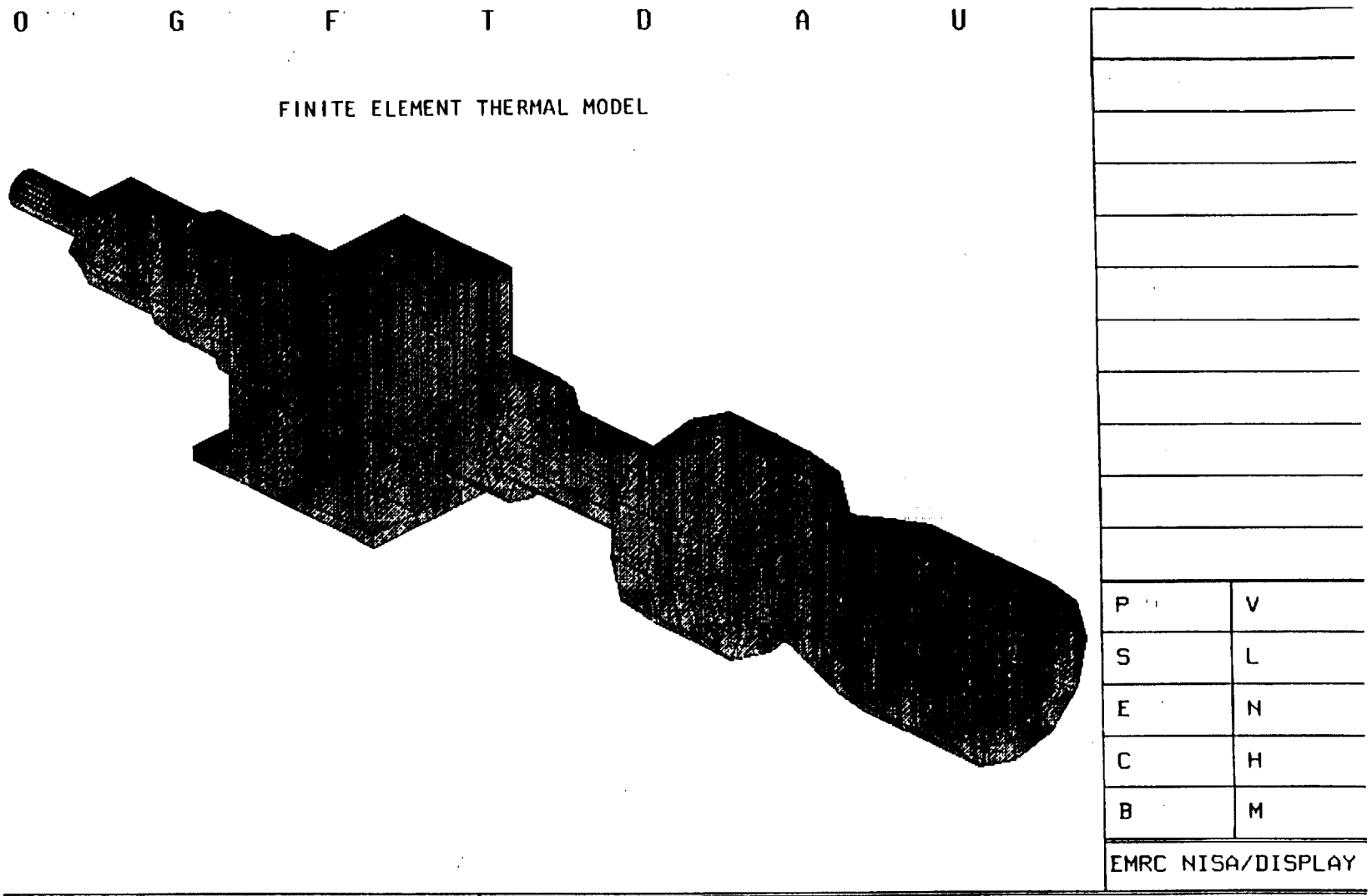
O G F T D A U
FINITE ELEMENT THERMAL MODEL
P V
S L
E N
C H
B M
EMRC NISA/DISPLAY
COMMAND> plo
COMMAND> vew.res
COMMAND> plo
Y
X
Z
X= 30
Y= -45
Z= 0

Figure 3-7

Runs were made with both a natural exterior with an emissivity of 0.2 and a spray coated exterior with an emissivity of 0.6. None of the critical temperatures were exceeded in either case, and for the 0.2 emissivity case, the gas temperature was increased by 200°F. As a result, it was decided to not coat the exterior.

The final predicted temperatures are shown in Figure 3-8. It should be noted that the greatest uncertainty in the model predictions is a result of the inability to precisely know how much power is input to the thruster structure during firing. RRC has correlated thermal model predictions with measured results on low power arcjets, and has achieved excellent agreement after several iterations. However, this kind of iterative process to refine the thermal model was beyond the scope of this program. This should be considered for future work so that the model predictions can be used to optimize the design. In this program, the model results were used to target key potential problem areas, but were not intended to provide exact temperature predictions.

4.0 Test Facilities/Procedures

Testing was performed in Cell 11 of the RRC Electric Propulsion Test Facility. A vacuum environment for arcjet operation is established by either one or two Stokes Model 1729 mechanical pumps. A plot of vacuum level as a function of hydrogen mass flow is shown in Figure 4-1.

Electrical power to the arcjet was supplied with a Hypertherm MAX 100 Plasma Cutting DC Power Supply. The output power level and on/off was controlled remotely from the control room. As shown in Figure 4-2, the electrical power circuit includes additional components used for the start up procedure. A capacitive high voltage start circuit is located in parallel with the DC output power leads to generate the voltage levels required for arc breakdown between the electrodes.

The hydrogen propellant was of Grade 4.7 (99.997 % purity) contained in industrial type high pressure cylinders. A pressure regulator located at the outlet of the cylinder was used to maintain an adequate pressure level into the system. A Micro-Motion Model D-6 was used as the mass flow meter. Remote flow control was accomplished by adjusting an electric motor attached to the shaft of a pressure regulator. A schematic of the propellant system is shown in Figure 4-3.

FINAL THERMAL MODEL PREDICTIONS

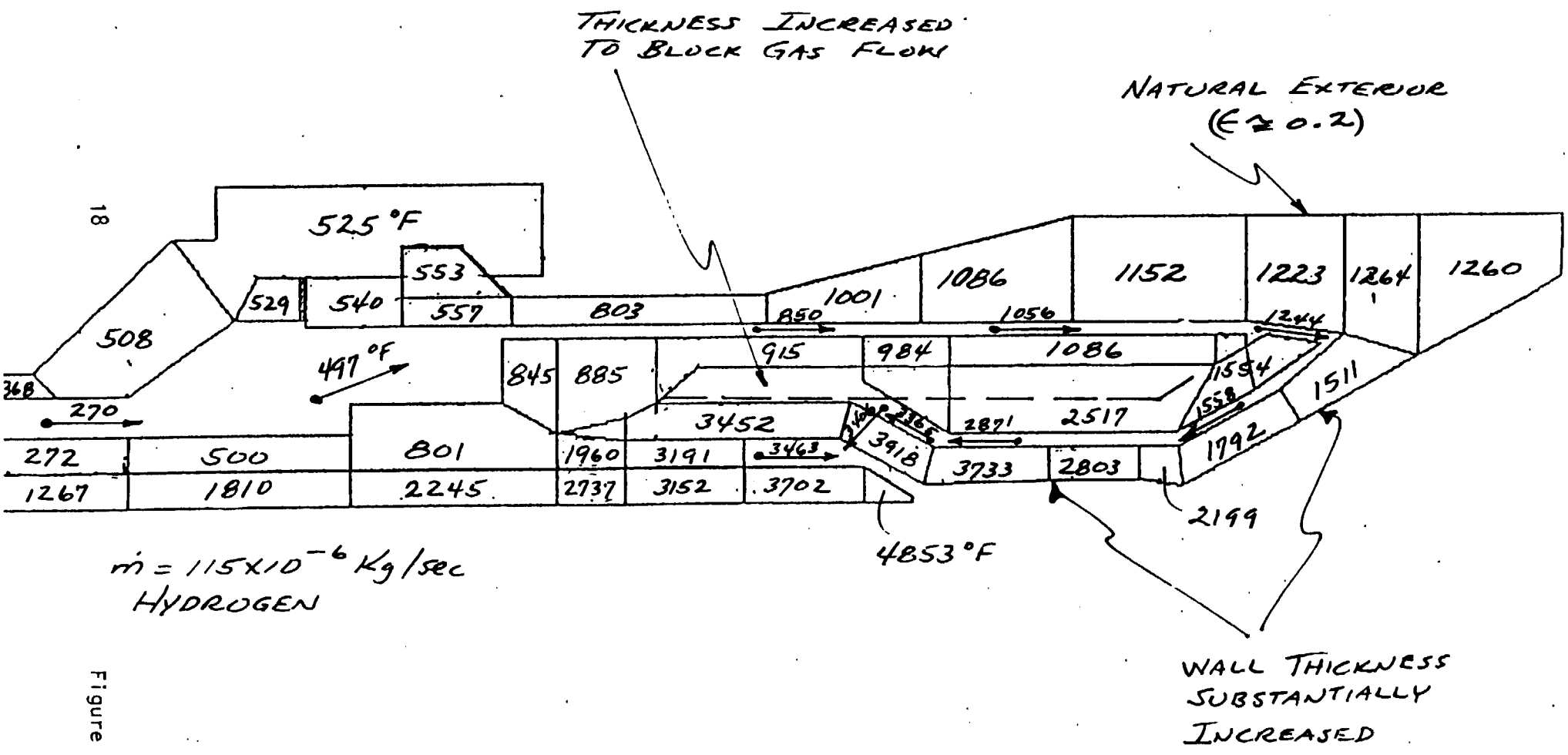

Figure 3-8

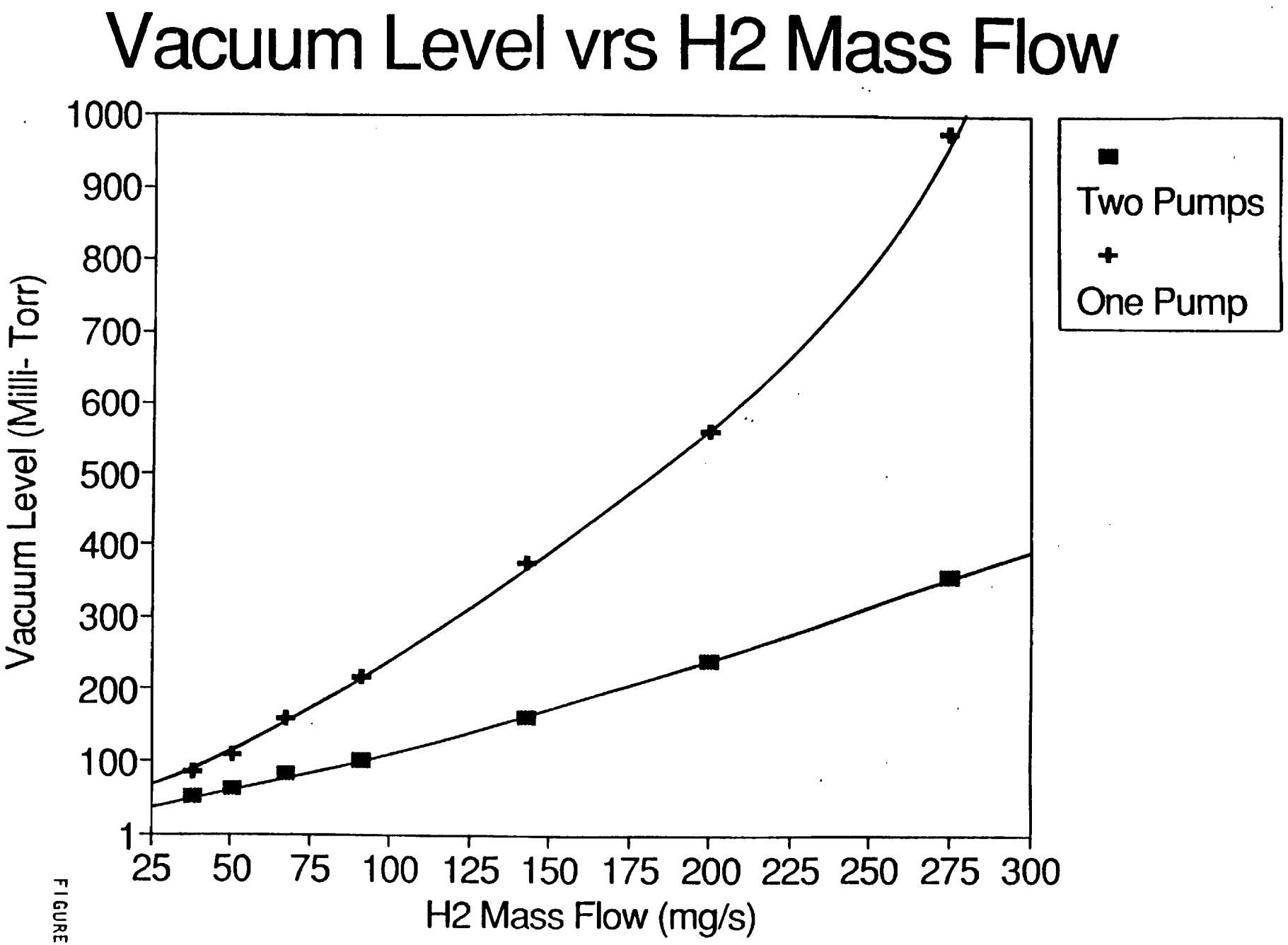
Vacuum Level vrs H2 Mass Flow
Vacuum Level (Milli- Torr)
1000
900
800
700
600
500
400
300
200
100
1
25
50
75
100
125
150
175
200
225
250
275
300
H2 Mass Flow (mg/s)
Two Pumps
One Pump

FIGURE 4-1

ELECTRICAL POWER DELIVERY SCHEMATIC

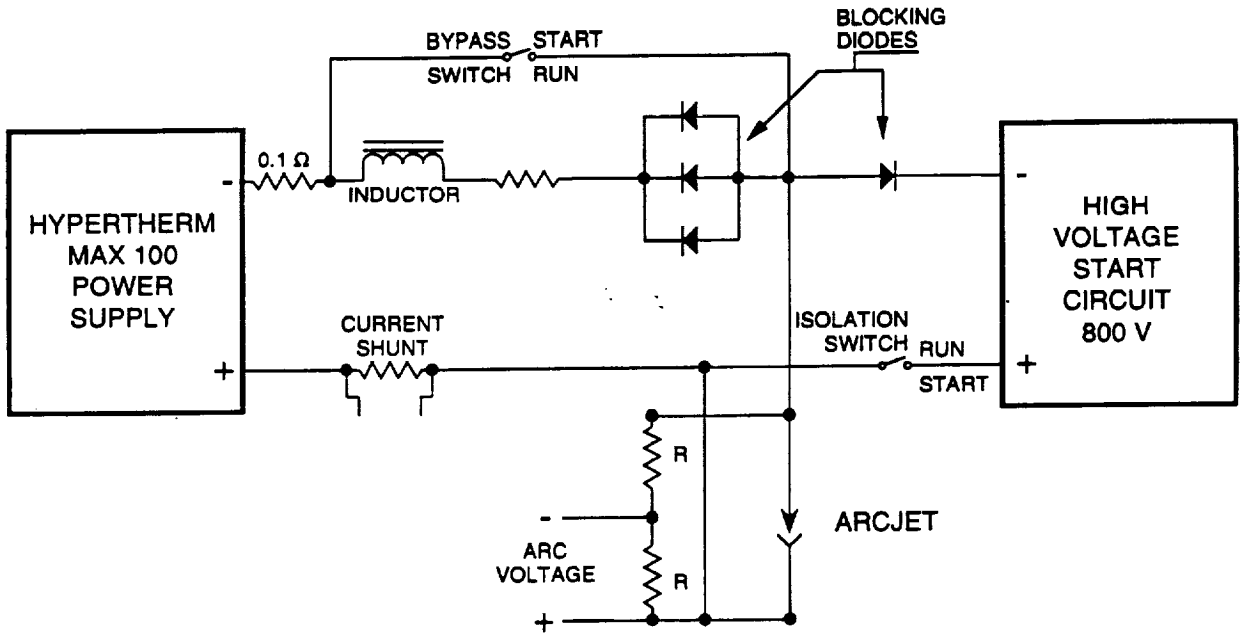

Figure 4-2

C11236-40

GIANNINI ARCJET PROPELLANT SCHEMATIC

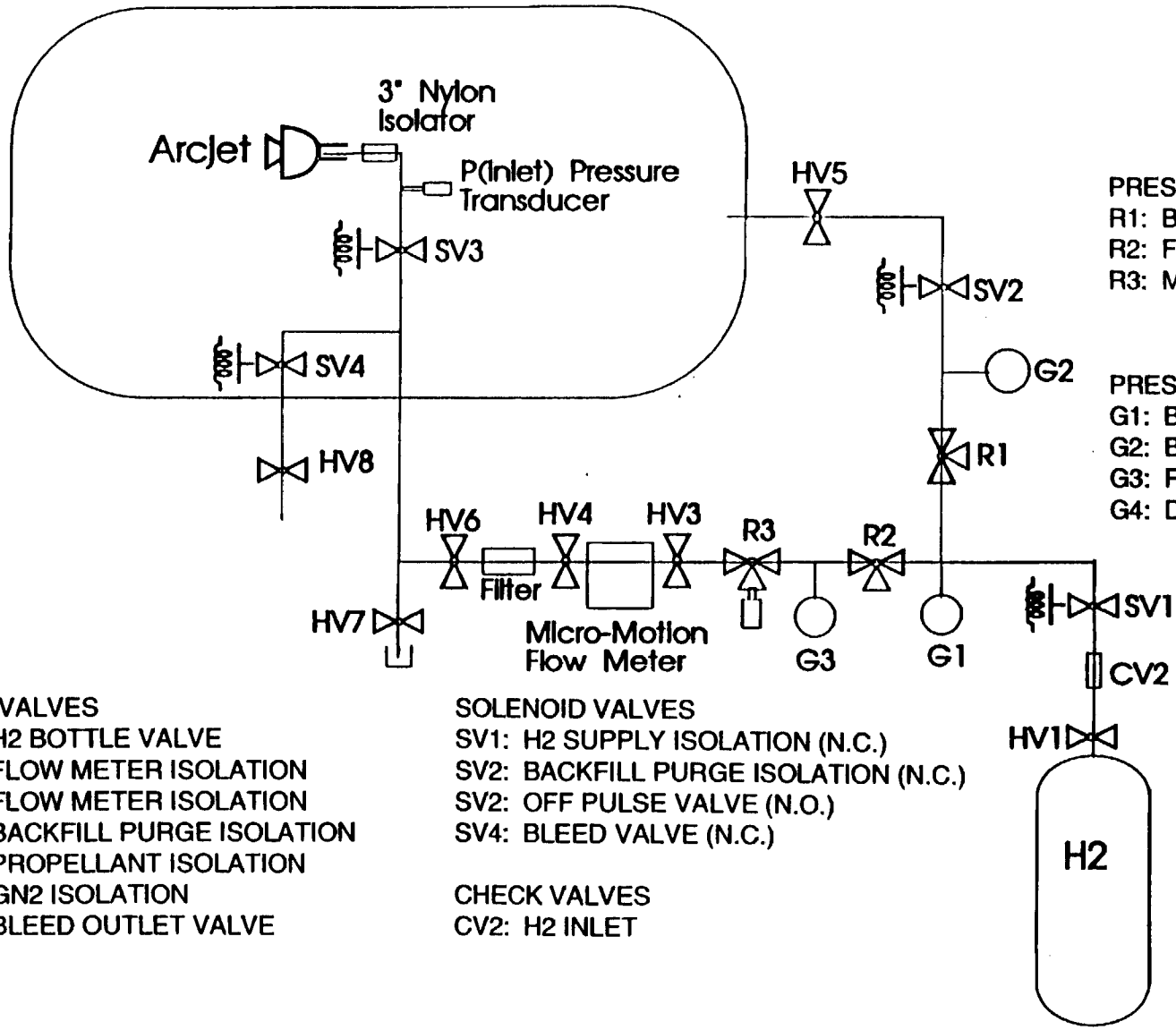

PRESSURE REGULATORS
R1: BACKFILL PURGE
R2: FEED PRESSURE
R3: MOTORIZED FLOW CONTROL

PRESSURE GAUGES
G1: BOTTLE PRESSURE
G2: BACKFILL PURGE PRESSURE
G3: R3 FEED PRESSURE
G4: D2 BOTTLE PRESSURE

HAND VALVES
HV1: H2 BOTTLE VALVE
HV3: FLOW METER ISOLATION
HV4: FLOW METER ISOLATION
HV5: BACKFILL PURGE ISOLATION
HV6: PROPELLANT ISOLATION
HV7: GN2 ISOLATION
HV8: BLEED OUTLET VALVE

SOLENOID VALVES
SV1: H2 SUPPLY ISOLATION (N.C.)
SV2: BACKFILL PURGE ISOLATION (N.C.)
SV2: OFF PULSE VALVE (N.O.)
SV4: BLEED VALVE (N.C.)

CHECK VALVES
CV2: H2 INLET

Figure 4-3

Data were continuously displayed and were also recorded at timed intervals on a PC based computer controller system. Strip chart recorders were used to record signals that require a graphical display to monitor transients and noise levels. The instrumentation list is shown in Table 4-1.

Table 4-1
Instrumentation List

Parameter	Range	Accuracy	Device
arc voltage	0 - 400 vdc	+/- 1.0%	1000:1 resistive voltage divider
arc current	0 - 100 amps	+/- 1.0%	300 amp resistive current shunt
thrust	0 - 2.0 N	null balance	+/- 1.5%
propellant mass flow	0 - 200 mg/s	+/- 1.0%	Micro-Motion Model D-6
arcjet inlet pressure	0 - 200 psia	+/- 0.5%	Statham pressure transducer
vacuum tank pressure	0 - 1 Torr	+/- 5%	MKS Baratron vacuum gauge
arcjet temperatures	2300 F max.	+/- 0.75%	Type K thermocouples

Prior to the first augmented firing of the arcjet and at times throughout the test firings, several cold H_2 flow sequences were performed. Plots of cold flow thrust, inlet pressure, and mass flow were generated and maintained throughout testing as an indication of potential changes in the nozzle geometry or of the development of gas leaks. The cold flow tests were performed with thruster temperatures below 200°F to minimize the effectof gas heating on the performance parameters.

Prior to operating the arcjet with the DC power supply, a test is conducted at nominal mass flow rates which verifies that arc breakdown is occurring between the electrodes and not elsewhere in the electrical circuit. An arc discharge between the electrodes is generated by shutting off the mass flow for approximately 100 msec, which lowers the pressure within the nozzle enough to

create a Paschen breakdown. During this checkout procedure only the capacitive start circuit is used to minimize the potential for damage in case of an inadvertent breakdown.

Arcjet startup was accomplished by turning on the DC power supply at its maximum open circuit voltage level and creating a discharge as mentioned above. The capacitors sustain the arc until the DC power supply responds to the load and starts conducting and controlling current. Arc voltage and current start transient data were measured with a Tektronix P6015 broadband high voltage probe and a Tektronix A6303 current probe. Both signals were recorded with a Tektronix 2431L digital storage oscilloscope.

Power and mass flow rate are adjusted to obtain the desired power/mass flow ratio. Thermal equilibrium of the thruster typically requires 30 minutes of operation and is determined by monitoring temperature readings. Steady state performance measurements are recorded by averaging 300 samples, where each sample represents the average of 30 readings from the analog/digital board of the PC based controller. The time period for the recording process is roughly 10 seconds. Because of thermal zero shift of the thrust stand, performance measurements are obtained by using post-firing zeros as opposed to pre-firing zeros. Immediately after recording performance data at equilibrium conditions, the arc power is shut off, then the propellant valve located near the arcjet inlet is closed. Ten seconds elapse to allow residual gas to exit the arcjet nozzle prior to recording the post-firing zero thrust, inlet pressure, and mass flow rate measurements. The corrected engineering data are both recorded on a hard disk and printed.

5.0 Test Results

Performance data were taken over a range of power levels from 4 kW to 15 kW. Figure 5-1 shows I_{sp} vs. thrust efficiency over this range of power. Test firings at 4 kW to 6 kW resulted in thrust efficiencies greater than 50% and exhibited low anode surface temperatures, no visible exhaust plume, and stable operation. Increasing the power level at a fixed $P/\dot{m}$ level resulted in only slight improvements in efficiency. For example, increasing the power from 8 kW to 12 kW at 60 MJ/kg specific power caused the efficiency to increase from 49.5% to 51.2 %. Figure 5-2 shows the 10 kW data taken along with data from a standard constricted design tested by RRC on another program. At specific impulse levels below 950 sec the Giannini style thruster produced much higher efficiencies. However, above this performance level, the standard design was more efficient.

Isp Versus Efficiency

Hydrogen Propellant

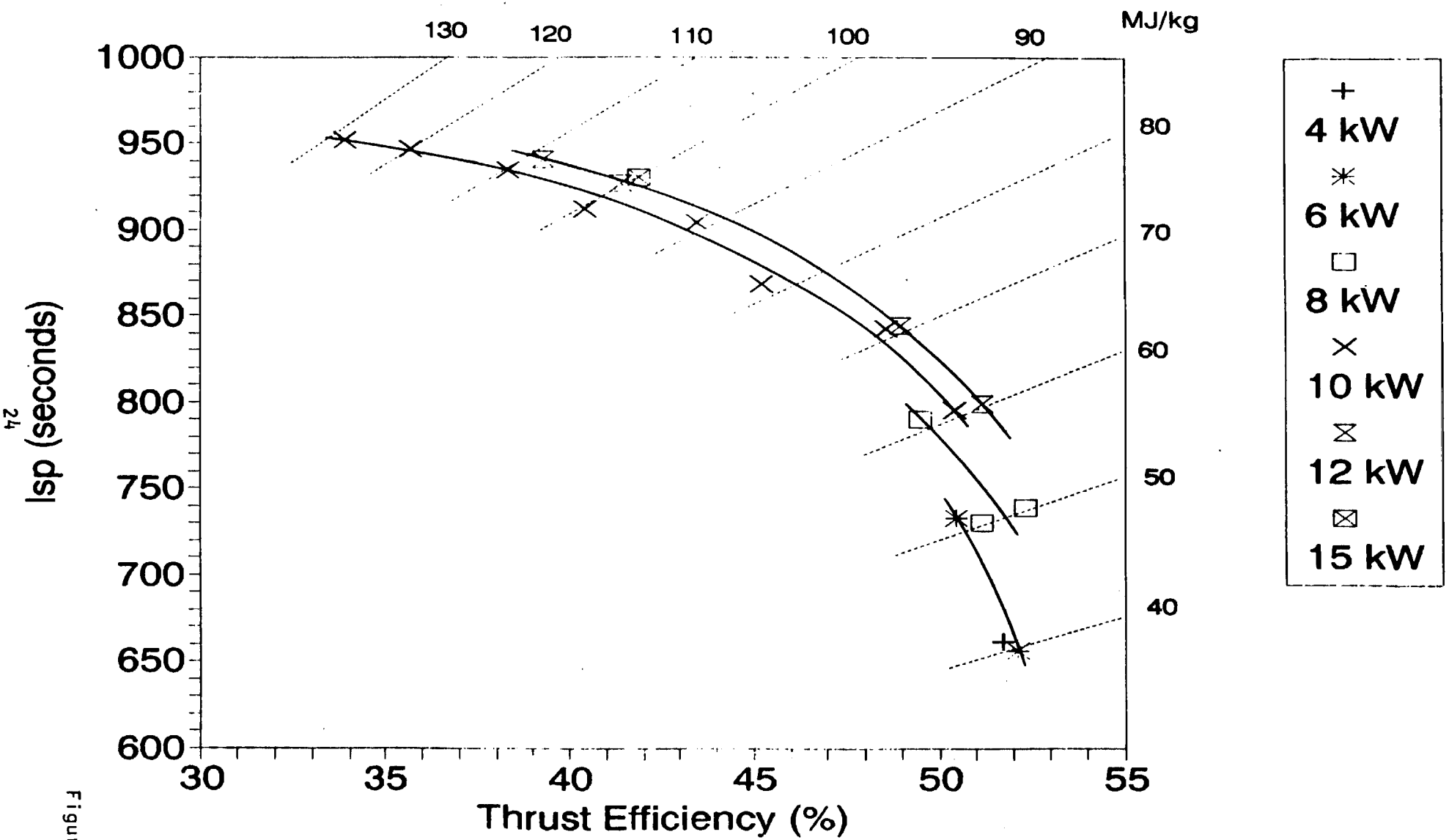

Figure 5-1

Isp Versus Efficiency

Hydrogen Propellant, 10kW

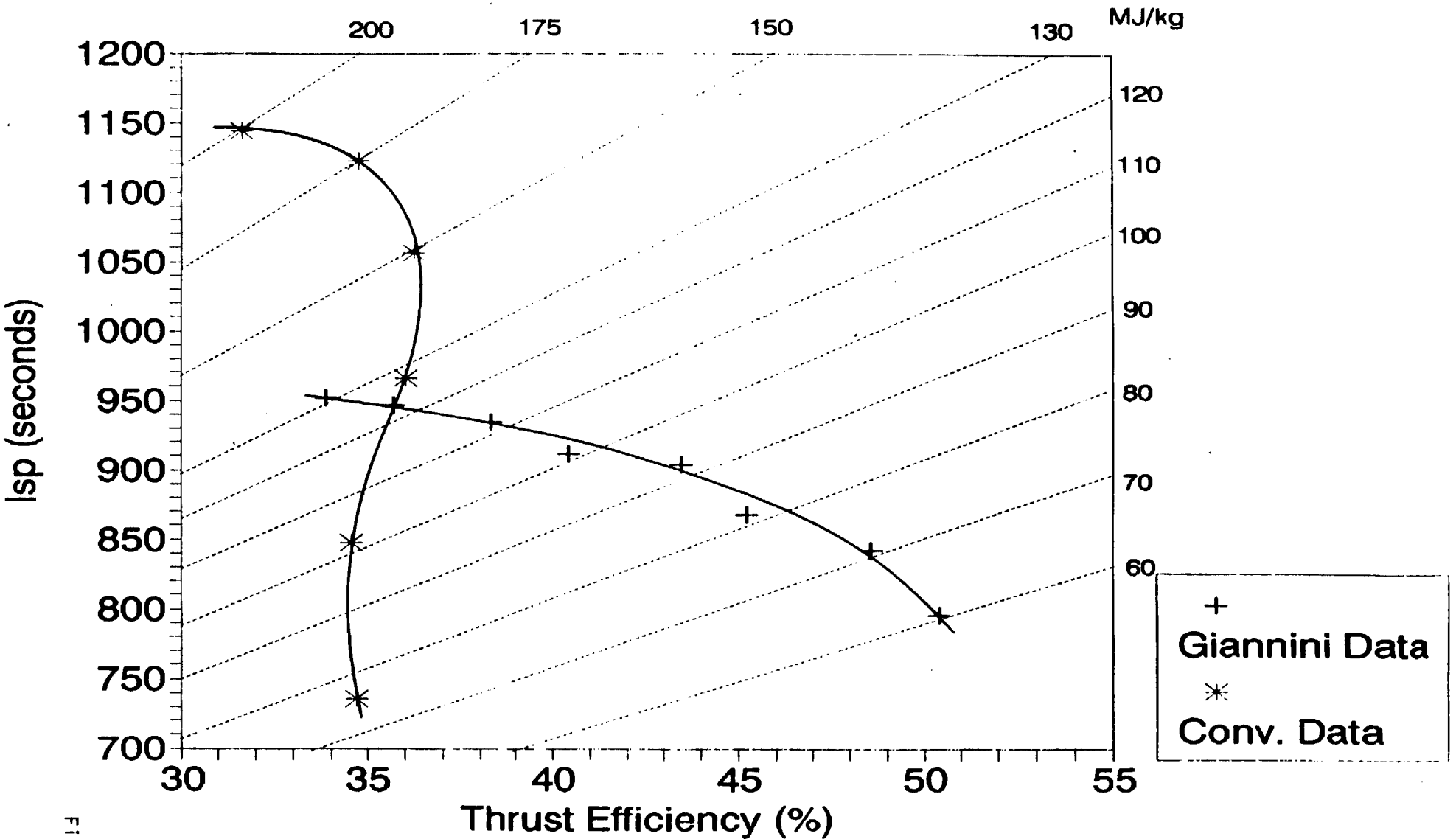

Figure 5-2

Figure 5-3 shows anode surface temperatures over a range of powers from 8 kW to 12 kW at a relatively low $P/\dot{m}$ level of 60 MJ/kg. The temperatures drop between 250°F and 400°F as the power and flow rate are increased. Although the heat loading is greater at 12 kW, the additional cooling by the increased mass flow results in lower temperatures. Figure 5-4 shows temperatures for a fixed power of 10 kW over a range of $P/\dot{m}$ levels. The temperatures climbed by close to 1000°F at the nozzle end as the $P/\dot{m}$ level was increased from 60 MJ/kg to 80 MJ/kg.

Voltage vs. current traces are shown in Figure 5-5. The range of voltages was between 120 V and 180 V. Figure 5-6 shows the arc voltage vs. flow rate. Apparently the arc voltage is directly dependent on the flow rate, and is not strongly dependent on the power level. Figure 5-7 shows the measured inlet pressure external to the thruster vs. mass flow rate.

A complete set of data from these tests is included in the appendix.

A boroscope was used periodically during testing to inspect the constrictor. This was recorded on a video tape. The surface finish was rougher just downstream of the small step in the constrictor, suggesting that this is where the arc was attaching. No erosion was observed. The throat region was recrystallized. Post-test inspection of the disassembled hardware indicated no difference from the boroscope findings.

6.0 Discussion

The main issue based on the test data is to determine why the efficiency drops off so rapidly as the $P/\dot{m}$ level is increased. Two approaches were taken to attempt to better understand this behavior.

During testing, the thrust level was recorded just after the arc was extinguished but with the flow still on. Using this and the end-of-run corrected total thrust, a measure of the amount of heat picked up from the structure by the gas can be obtained. The thrust measured just after the arc is shut off is in essence due to the resistojet-like behavior of the thruster. This thrust level can be correlated with an enthalpy level using the CEC chemical kinetics program . This provides an estimate of the total power being absorbed by the gas from the flow passages by multiplying the enthalpy by the mass flow rate.

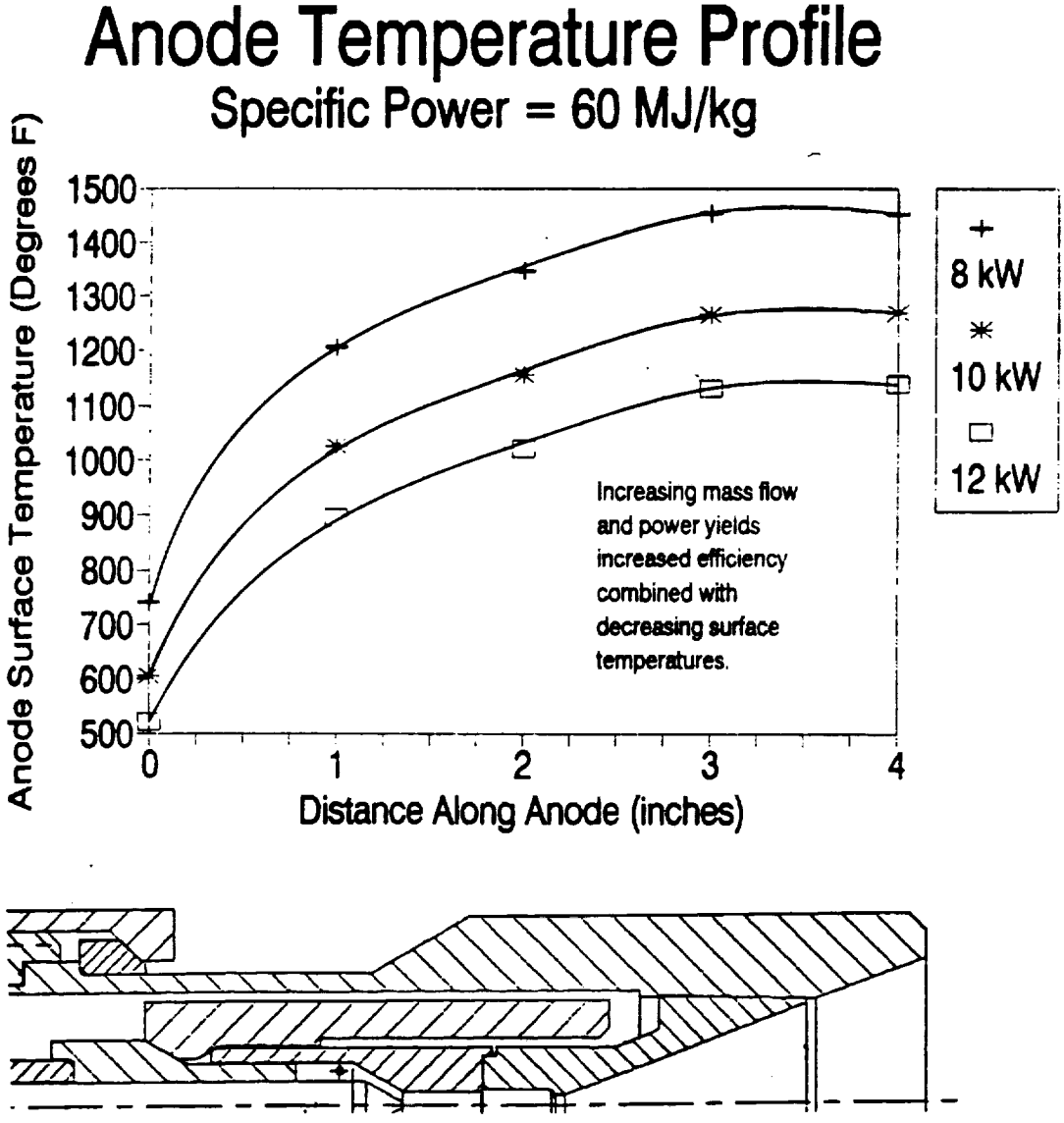
Anode Temperature Profile
Specific Power = 60 MJ/kg
Anode Surface Temperature (Degrees F)
1500
1400
1300
1200
1100
1000
900
800
700
600
500
0
1
2
3
4
Distance Along Anode (inches)
8 kW
10 kW
12 kW
Increasing mass flow and power yields increased efficiency combined with decreasing surface temperatures.

Figure 5-3

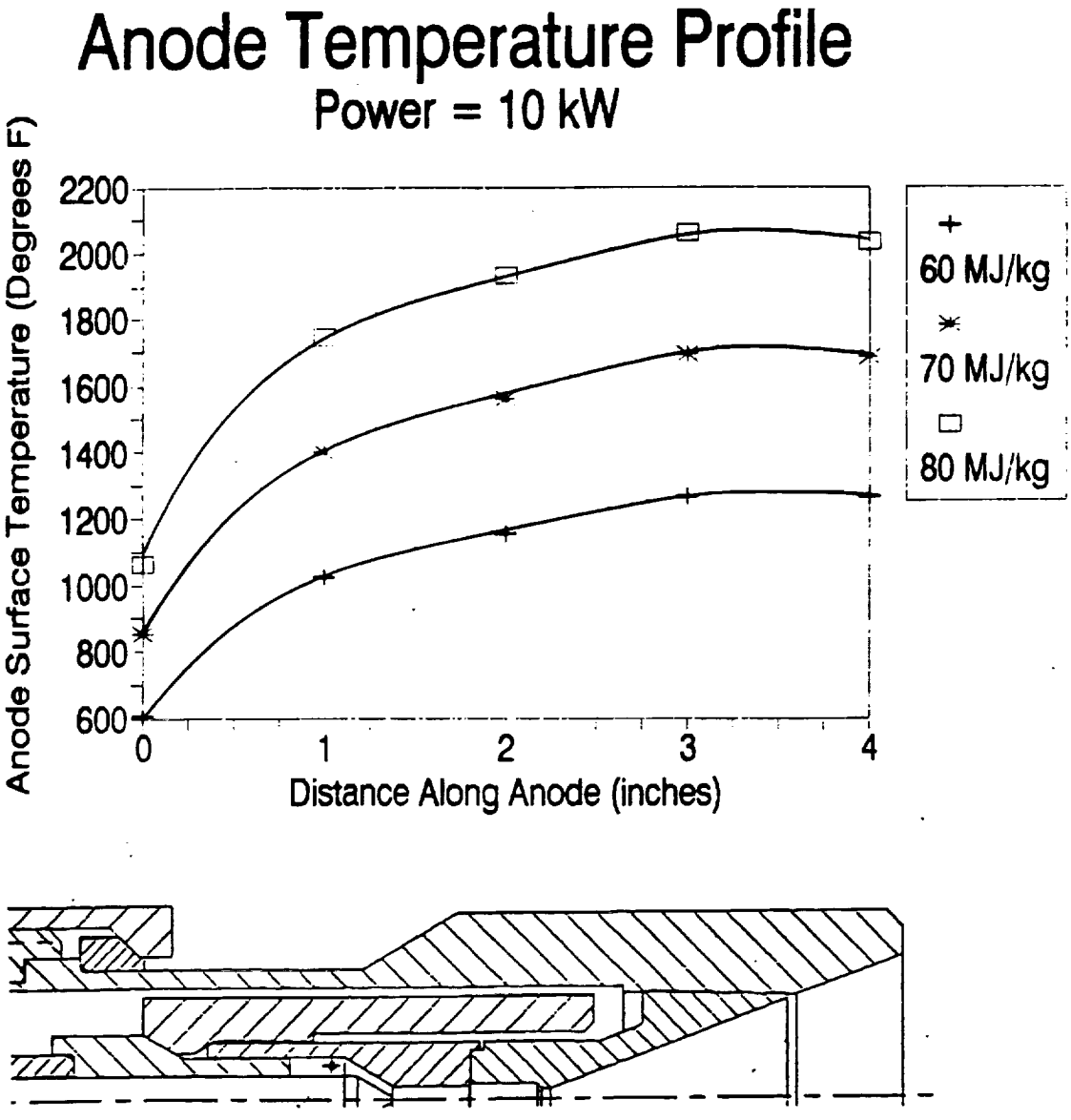
Anode Temperature Profile
Power = 10 kW
Anode Surface Temperature (Degrees F)
2200
2000
1800
1600
1400
1200
1000
800
600
0
1
2
3
4
Distance Along Anode (inches)
60 MJ/kg
70 MJ/kg
80 MJ/kg

Figure 5-4

Arc Voltage versus Arc Current

Hydrogen Propellant

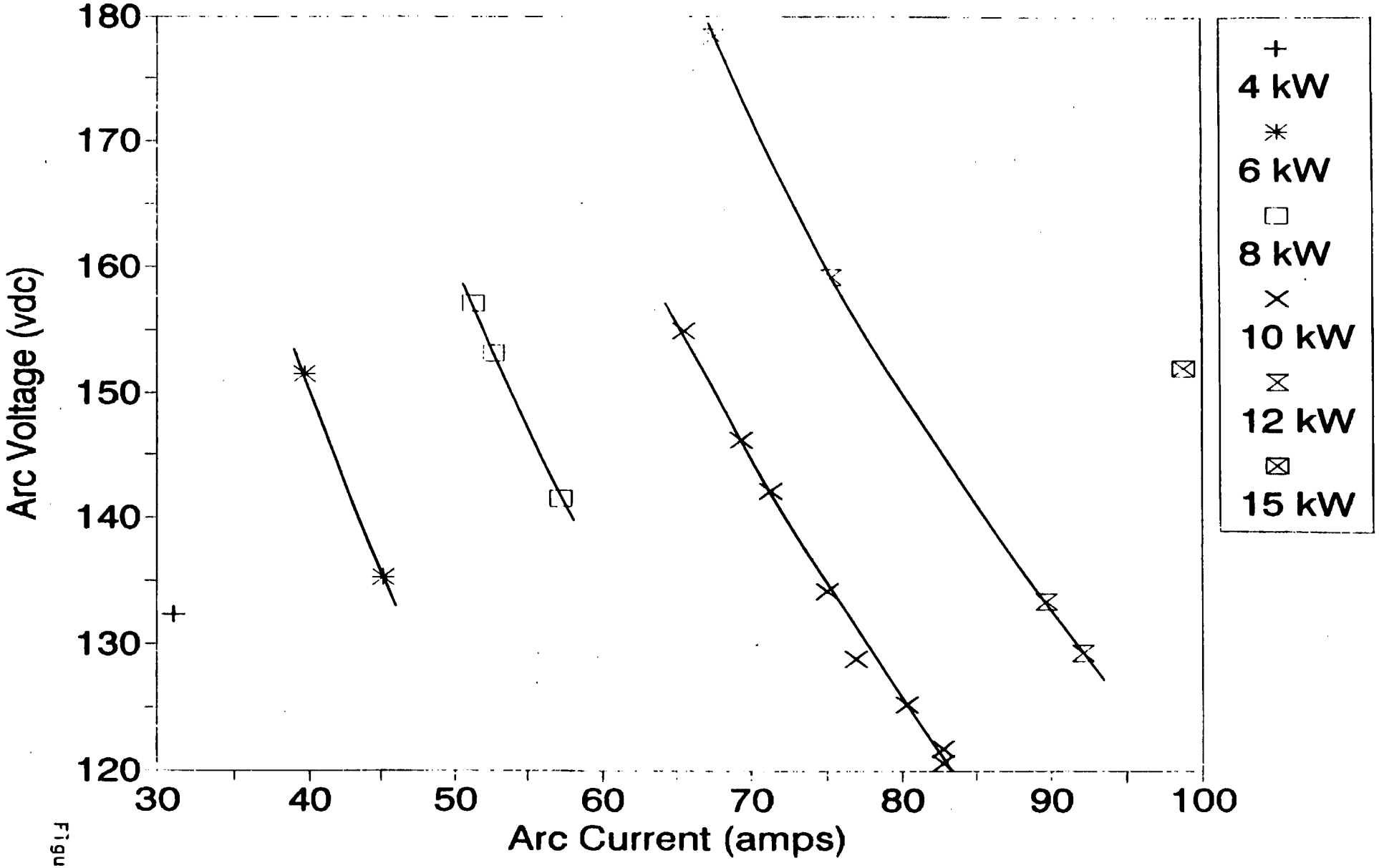

Figure 5-5

Arc Voltage versus Mass Flow Rate

Hydrogen Propellant

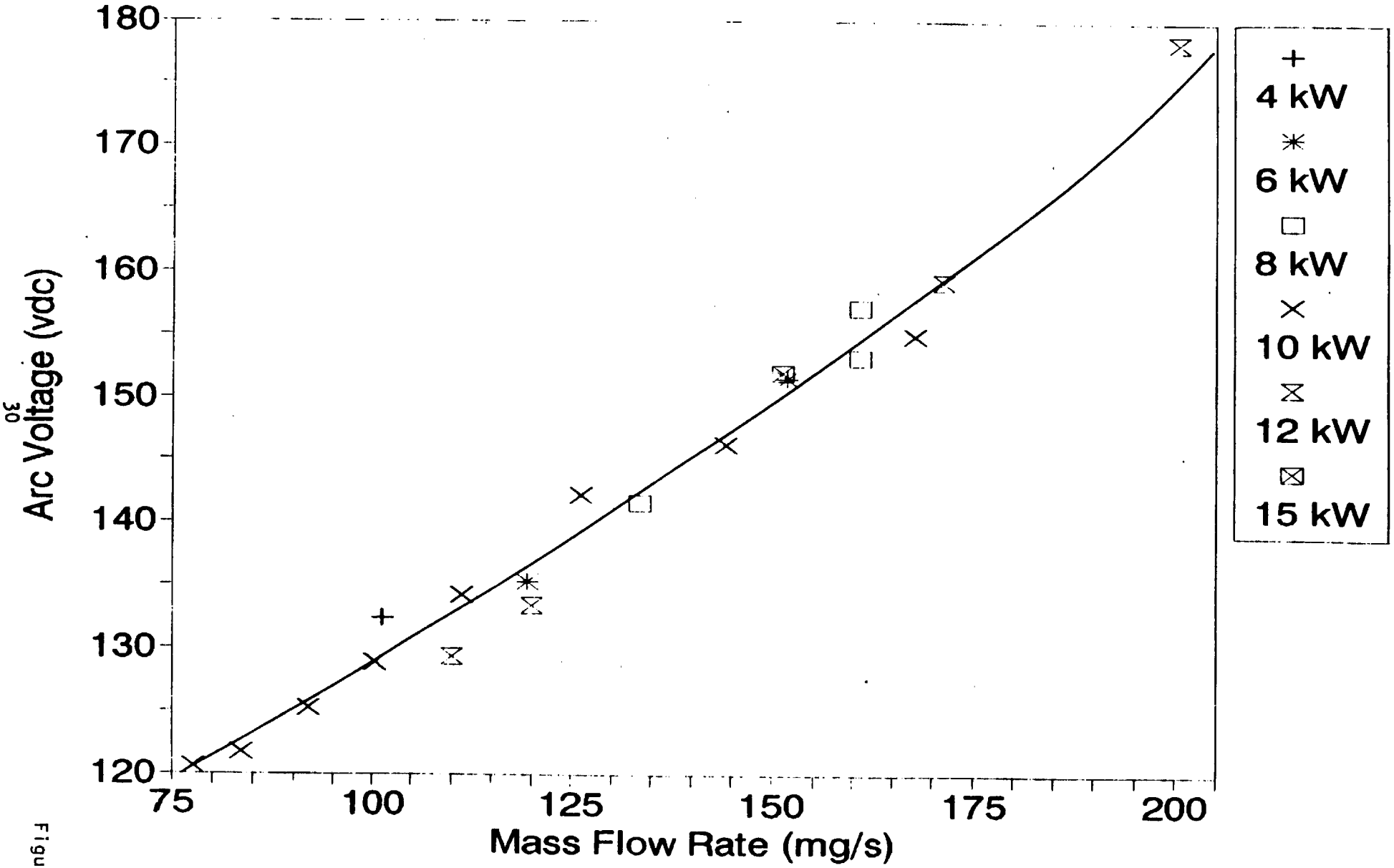

Figure 5-6

Inlet Pressure versus Mass Flow Rate

Hydrogen Propellant

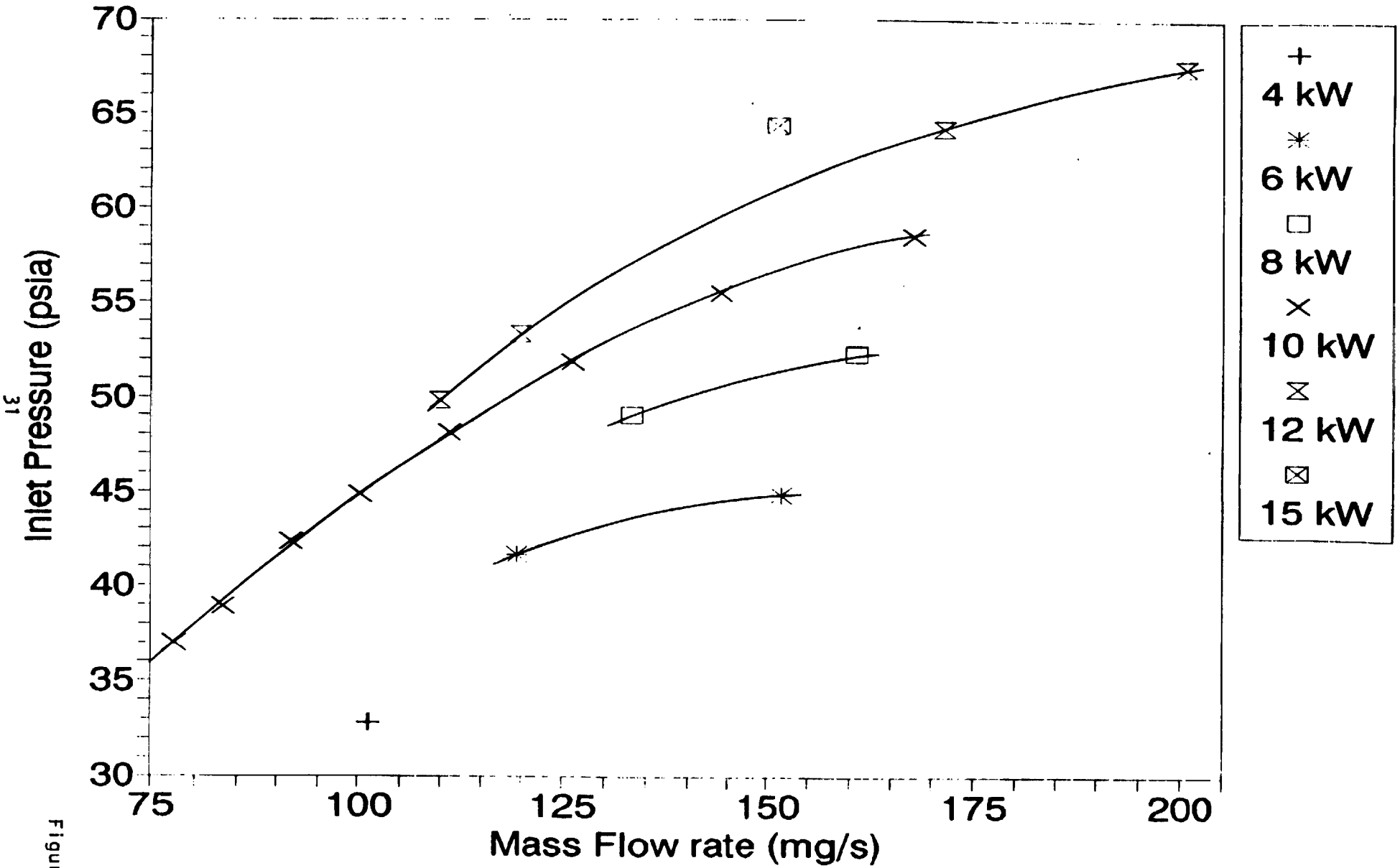

Figure 5-7

Figure 6-1 shows the predicted I_{sp} as a function of enthalpy based on CEC model runs, assuming that the flow is in equilibrium upstream of the throat and frozen downstream of the throat. Subtracting a small amount of enthalpy contained in the ambient temperature inlet gas provides a total enthalpy increase. Multiplying by the flow rate gives the total power picked up by the gas. Table 6-1 shows the measured I_{sp} levels just after the arc was shut off, and the calculated values of delta enthalpy and power. The estimated gas temperature upstream of the throat is also included. Figure 6-2 shows the arc-off I_{sp} vs. specific power. The calculated power is graphed against $P/\dot{m}$ in Figure 6-3.

Several observations can be made based on this approach. First, the estimated gas temperatures are in a range of 1400°F to 2450°F. External temperatures were measured to over 2500°F, and thermal modeling predicts that the temperature difference between the outer wall and the constrictor should be 1000-2000+°F. In addition, pyrometer measurements taken looking up the nozzle indicated temperatures in excess of 3500°F at the high specific power levels. This evidence suggests that the constrictor walls are substantially hotter than the gas after the arc is shut off, which means that there is room for improvement in the effectiveness of the heat exchanger. This will be addressed in the recommendations section.

A second observation is that there is a distinct maximum in the power absorbed by the gas as a function of $P/\dot{m}$. The gas temperature increases as the $P/\dot{m}$ level is raised. However, above a $P/\dot{m}$ level of about 80 MJ/kg, the drop in flow rate results in a reduced total power being absorbed by the gas. As a result, the increased thermal losses that occur at higher $P/\dot{m}$ levels are compounded by the fact that less of the available energy can be recovered by the gas through the regenerative passages.

A second approach taken to better understand the rapid decrease in efficiency as $P/\dot{m}$ was increased was to estimate the radiation losses from the thruster body. This was done by dividing the body into 3 distinct regions, and selecting an average temperature for each region based on thermocouple measurements. Data were not available for all operating points because at higher $P/\dot{m}$ levels, the temperatures exceeded the limits of the type K thermocouples. Nonetheless, estimates were made for 5 of the operating points.

A key variable is the emissivity. The hemispherical total emittance of molybdenum increases with temperature. At 1340°F (1000 K), the emittance ranges from 0.10 to 0.15 for polished molybdenum. At 2420°F (1600 K), the emittance ranges from 0.15 to 0.20. Since the exact

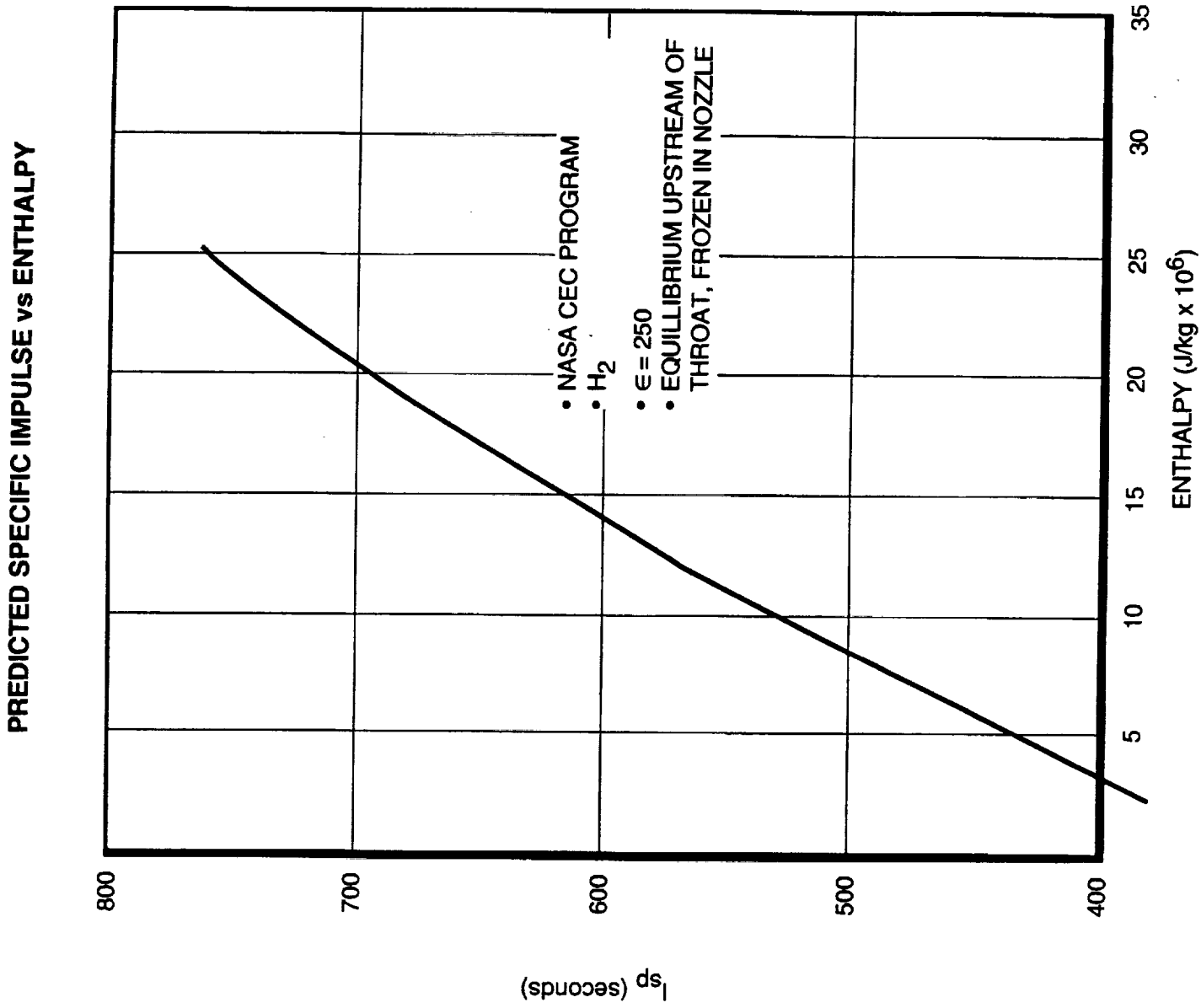

Figure 6-1

C11236-39

Table 6-1
REGENERATIVE THRUST DATA, 10 kW

Data Point No.	Power (kW)	Isp Arc-On (sec)	η Arc-On (%)	P/$\dot{m}$ (MJ/kg)	Isp Arc-Off (sec)	Δ Isp (sec)	Enth CEC (MJ/kg)	Δ Enth (T_o = 70°F) (MJ/kg)	$\dot{m}$ (mg/s)	Gas Power (W)	Calculated T_{gas} (°F)
6	10.14	796	50.4	60.4	547	249	11.0	10.75	167.8	1803	1400
8	10.14	842	48.6	70.3	597	245	13.6	13.35	144.2	1925	1680
12	10.14	908	45.2	80.3	626	282	15.6	15.35	126.3	1938	1950
13	10.06	904	43.5	90.5	654	250	17.4	17.15	111.3	1908	2100
14	9.92	912	40.4	98.8	672	240	18.5	18.25	100.4	1832	2300
15	10.06	935	38.3	109.5	678	257	18.8	18.55	91.8	1702	2360
19	9.99	953	33.9	128.6	690	263	19.6	19.35	77.7	1503	2450

Arc Off Isp versus Specific Power

Hydrogen Propellant, 10 kW

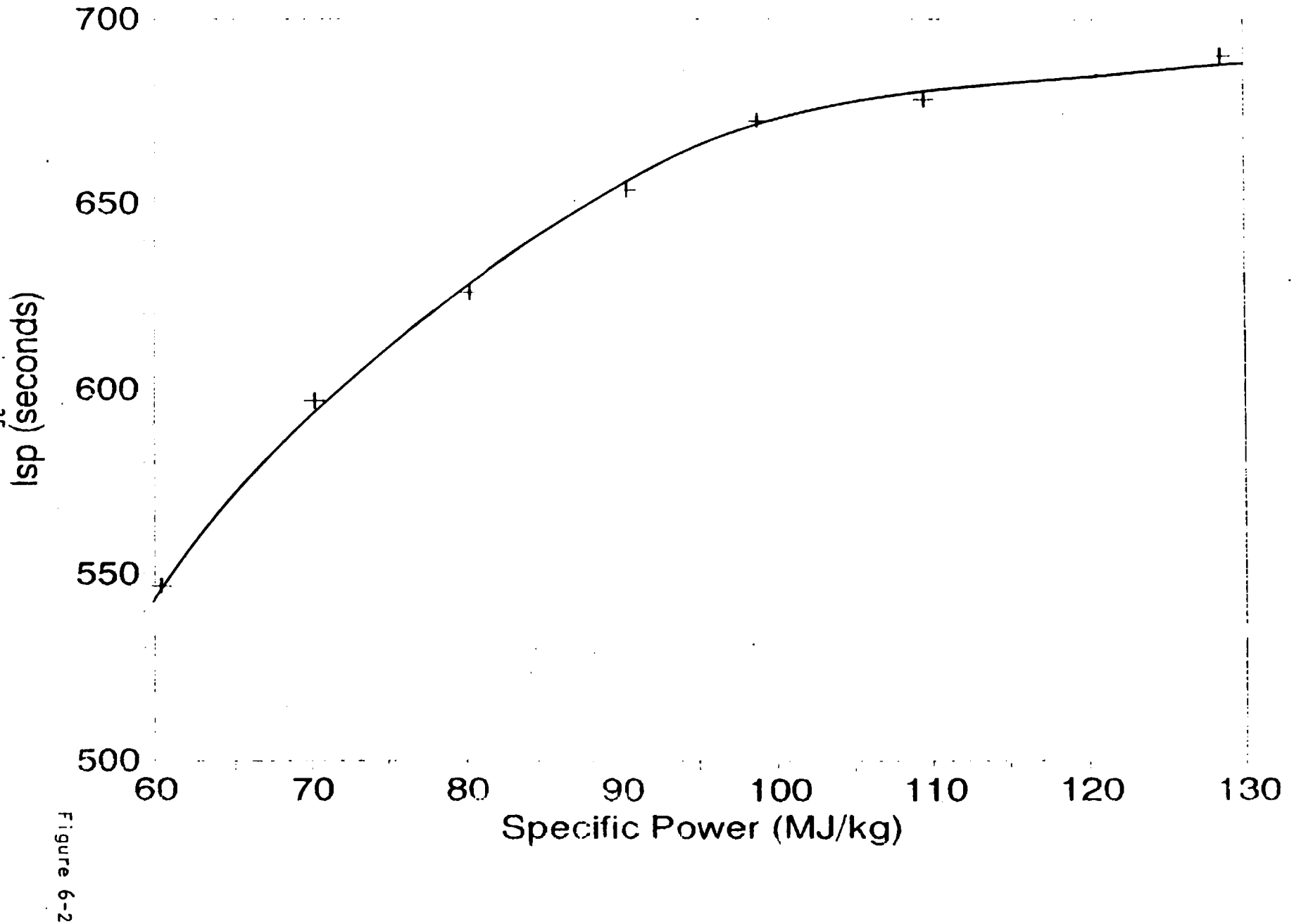

Figure 6-2

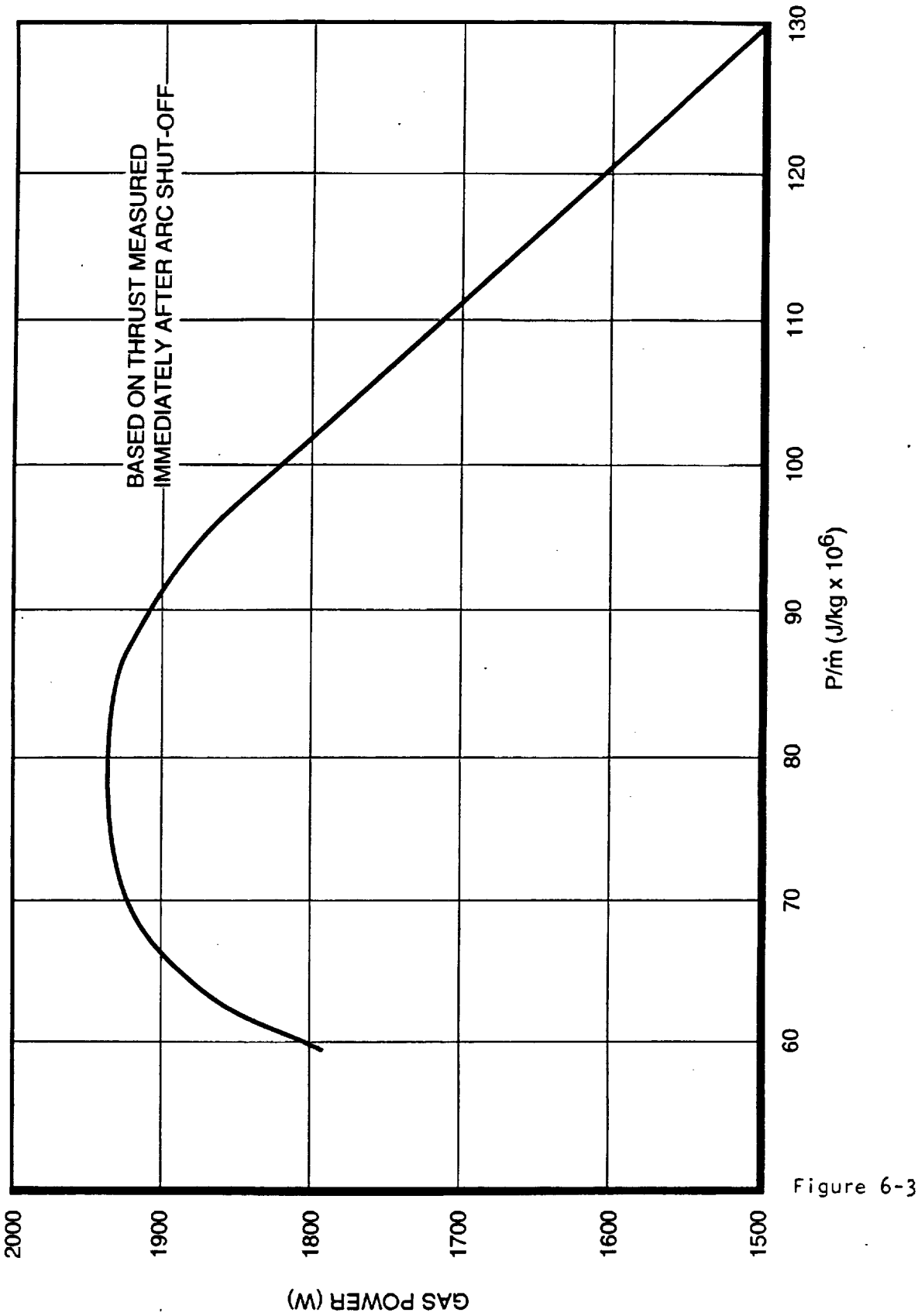

Figure 6-3

C11236-36

value was not determined experimentally, the calculations were performed over a range of values.

Figure 6-4 shows the locations of the thermocouples. The temperature data are included in the appendix. Table 6-2 shows the calculated radiation losses for assumed emittances of 0.15 and 0.20. A plot of radiative power vs. P/$\dot{m}$ is shown in Figure 6-5. It is apparent that these losses increase rapidly with increasing specific power. These calculations did not consider the heat conducted through the thruster, and are therefore a conservative estimate of the losses.

Table 6-2
Radiation Loss Estimates, 10 kW

Data Point #	P/mdot (MJ/kg)	Q_{rad} ϵ = 0.15 (W)	Q_{rad} ϵ = 0.20 (W)	
6	60.4	92	123	
8	70.3	222	296	
12	80.3	403	537	
13	90.5	644	859	
14	98.8	896	1195	
15	109.5	—	—	no temp data
19	128.6	—	—	no temp data

If the thruster efficiency drops from 40% to 30% at the same input power, this implies that 10% of the input power is no longer available as thrust. This energy could end up as frozen flow, or as thermal losses. It is not likely that such a large change could be due primarily to a decrease in nozzle efficiency. If all of it theoretically ended up as a thermal loss, this would define an upper bound for the slope of the thermal loss calculations. In other words, if at 10 kW the thruster lost 10 percentage points in efficiency, the maximum increase in the thermal losses would be 1.0 kW. Figure 6-6 shows the calculated radiative losses vs. thruster efficiency for the 5 points. Also shown are theoretical curves for both 100% and 50% of any additional losses being due to structural heating. From this graph it can be seen that a significant portion of the drop in efficiency must be due to increased thermal losses, even if the assumptions regarding the emissivity are not accurate. In the future, a shell model of the thruster could be constructed which would much more accurately calculate the radiative and conductive thermal losses.

THERMOCOUPLE LOCATIONS

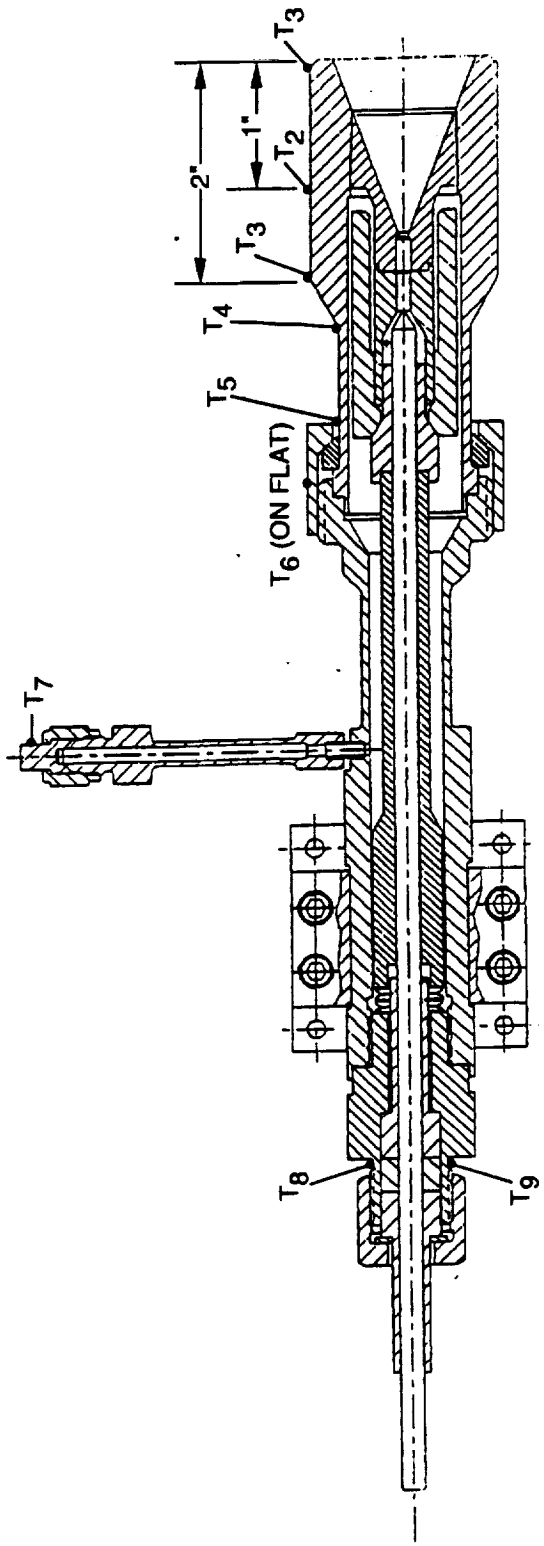

Figure 6-4

C11236-38

C11236-37

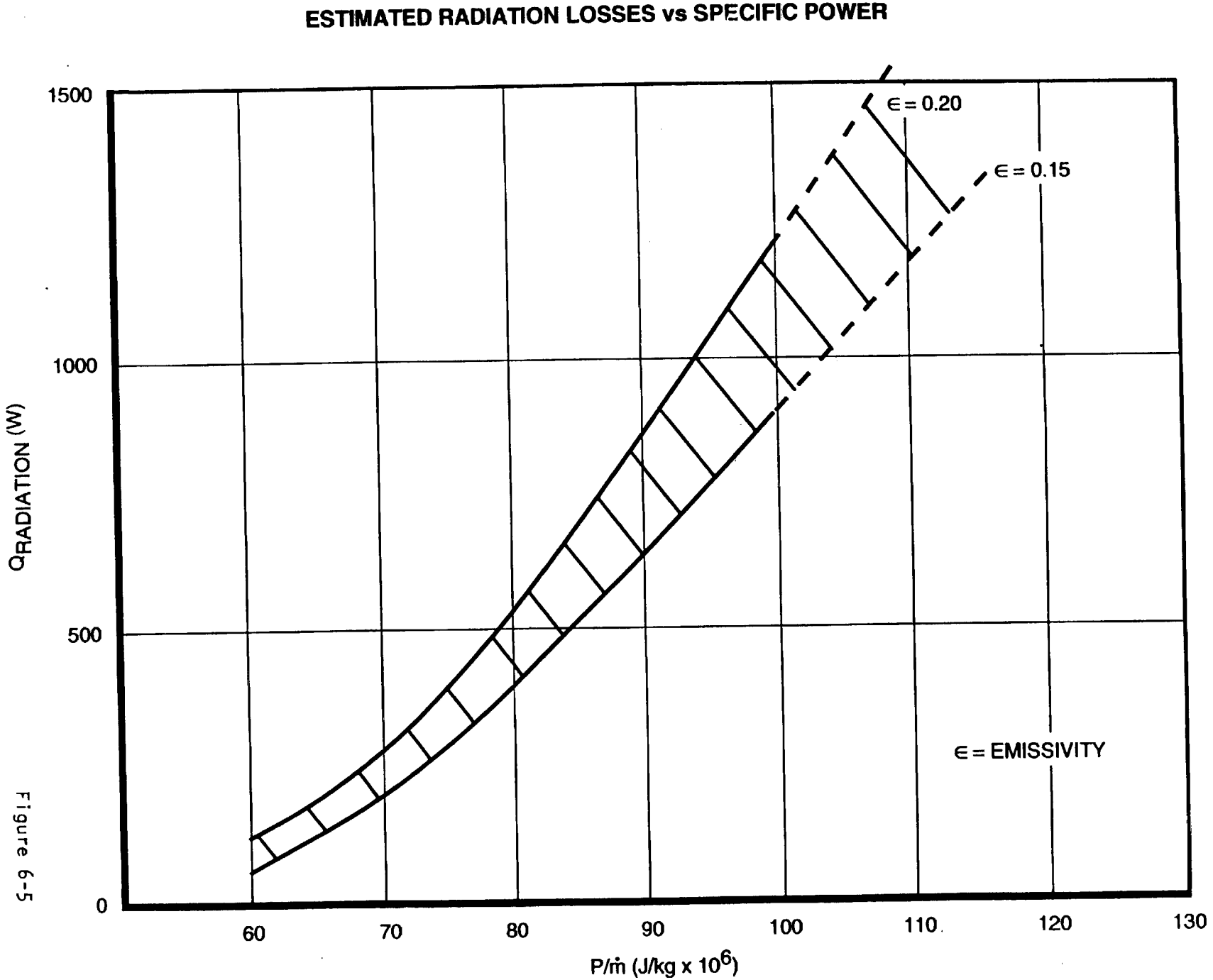

Figure 6-5

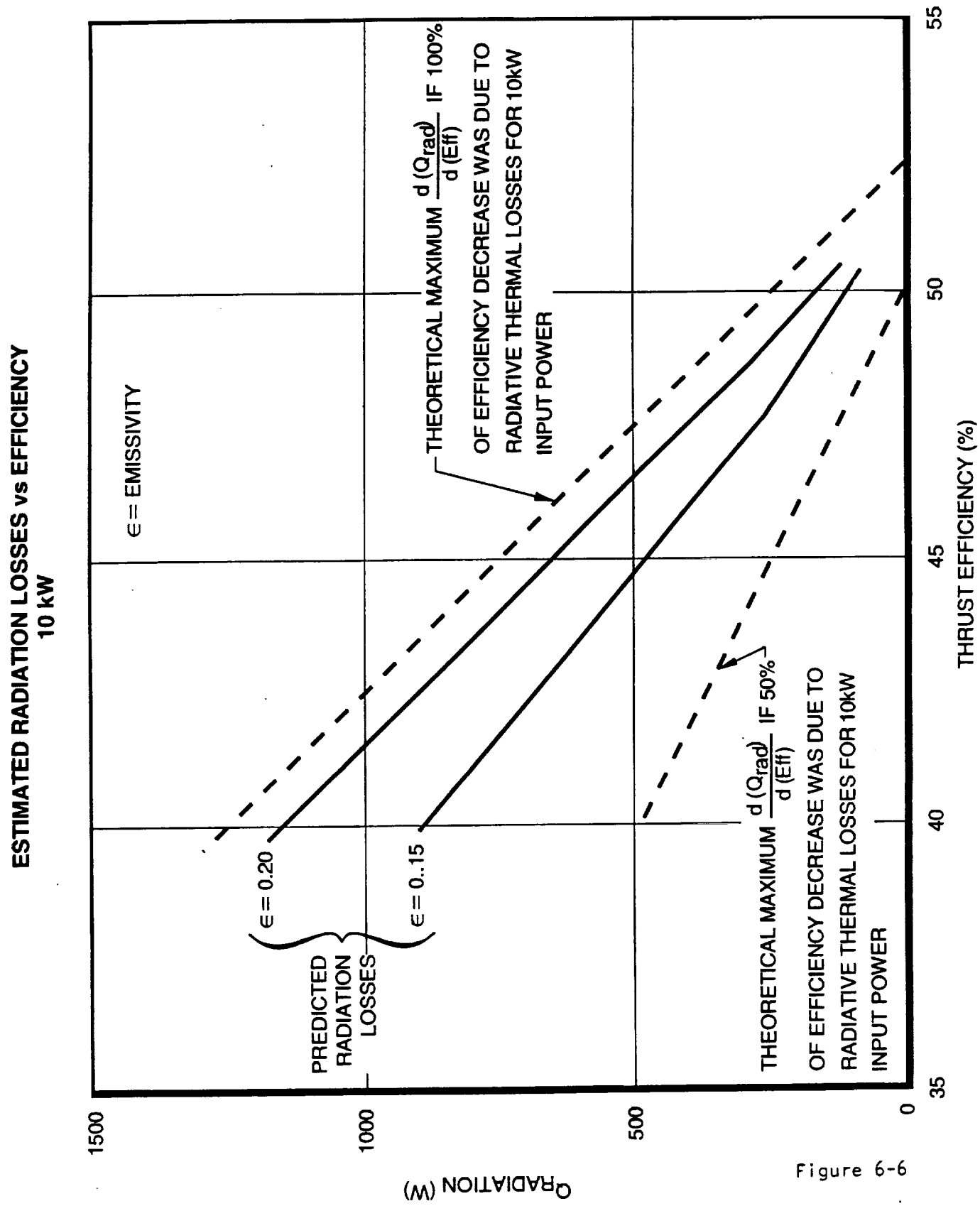

Figure 6-6

C11236-35

The point of this discussion is that design changes are needed to reduce the thermal losses at higher $P/\dot{m}$ levels. Combining the gas power and radiative loss estimates as a measure of the total power entering the structure shows that out of 10 kW input power, well over 3000 W are being deposited to the thruster walls at $P/\dot{m}$ levels above 100 MJ/kg. Although some of this is recovered by the gas, the ratio of gas power to radiative losses rapidly decreases as the specific power is increased. Some of the design recommendations discussed below are aimed at reducing these losses.

7.0 Conclusions/Recommendations

Testing of a scaled Giannini-style thruster was completed successfully, with data taken over a range of power levels from 4 kW to 15 kW. The thruster ran very stably, and no erosion was evident. Efficiencies much higher than conventional designs were achieved at specific impulse levels up to 950 sec. Unfortunately, operation at specific impulse levels of interest (>1000 sec) was not achieved because of a rapid decrease in efficiency as the specific power was increased. This was apparently due to a very rapid increase in the thermal losses.

There are several recommendations for future work. First, steps should be taken to reduce the thermal losses. Reducing the length and diameter of the constrictor/throat would lower the surface area which is in contact with the hot gases. Second, there is room for improving the heat exchanger efficiency. This could be done by reducing the anode nozzle wall thickness to raise the constrictor temperatures, and by improving the gas path to increase the surface area and resident time. Third, RRC recommends that a non-regenerative configuration, as was shown in Figure 3-6, be built and tested to investigate separately the effect of the subsonic constrictor. Fourth, a shell thermal model of the thruster should be constructed to allow more accurate calculations of thermal losses based on thermocouple and CID camera measurements. This would provide a way to measure the degree to which design changes have affected the thermal losses. Last, the dependence on power should be evaluated further by testing at higher powers of up to 20 kW.

References

1. Todd, J. P., Development of a Thermal Arcjet Engine, Plasmadyne Corp., June, 1961.
2. Todd, J.P., 30 kW Arcjet Thruster Research, Plasmadyne Corp., September, 1963.
3. Todd, J.P., 30 kW Arcjet Thruster Research, Plasmadyne Corp., March, 1964.

APPENDIX

TEST DATA

Sequence Number	Flow Lbm/S	Flow Mg/S	V dc Volts	I dc Amps	Fmeas Lbf	Pi Psi	Palt Mtorr
1	0.000223	101.3211	132.2955	31.13374	0.139293	32.7303	236.8376
2	0.000335	151.803	151.4958	39.84827	0.205577	44.86132	397.7277
3	0.000264	119.5525	135.2283	45.24232	0.182848	41.63022	291.2498
4	0.000355	160.8578	153.0561	52.64854	0.252486	52.30945	179.1006
5	0.000294	133.4577	141.5531	57.28887	0.22745	49.04218	144.1972
6	0.00037	167.8113	154.8125	65.5138	0.278107	58.5288	461.0111
7	0.000442	200.5729	178.3455	67.48161	0.344798	67.46824	236.4368
8	0.000318	144.2031	146.1838	69.3347	0.254849	55.47571	367.4043
9	0.000355	160.8058	157.011	51.36271	0.246693	52.21359	428.6008
10	0.000378	171.4468	159.1883	75.39151	0.302415	64.19507	472.1363
12	0.000278	126.3205	142.1389	71.31388	0.231123	51.82555	302.9857
13	0.000245	111.2806	134.1751	75.0082	0.217638	48.09936	116.4836
14	0.000221	100.3591	128.8008	77.00857	0.19799	44.79471	104.0569
15	0.000202	91.83726	125.1472	80.37321	0.185782	42.32375	95.07821
16	0.000265	120.0089	133.335	89.74488	0.240676	53.26942	126.2188
17	0.000243	110.0892	129.2315	92.21077	0.224216	49.76715	114.7412
18	0.000184	83.41754	121.7018	82.74973	0.17104	38.93961	86.34416
19	0.000171	77.67649	120.577	82.81123	0.160114	36.96138	80.6832
20	0.000334	151.2817	151.8967	98.83682	0.296223	64.35002	392.6891

Sequence Number	F P*A Lbf	Ftotcorr Lbf	F PA% Pcnt	IsptotCor seconds	EffCorr Percent	Power Watts	MJ/Kg
1	0.008332	0.147625	5.981779	660.8832	51.70845	4118.853	40.65839
2	0.013992	0.219569	6.806428	656.0798	52.09212	6036.845	39.77439
3	0.010246	0.193094	5.603819	732.6151	50.47616	6118.042	51.18324
4	0.006301	0.258787	2.495551	729.7367	51.15945	8058.18	50.10359
5	0.005073	0.232523	2.230378	790.2925	49.46728	8109.417	60.77431
6	0.016219	0.294326	5.831859	795.5594	50.39829	10142.36	60.44936
7	0.008318	0.353116	2.412446	798.5656	51.14866	12035.04	60.01354
8	0.012926	0.267775	5.071885	842.2876	48.57737	10135.61	70.29899
9	0.015079	0.261771	6.112301	738.3891	52.32181	8064.509	50.15913
10	0.01661	0.319025	5.492529	844.0346	48.9784	12001.45	70.01292
12	0.010659	0.241782	4.611981	868.1919	45.20708	10136.48	80.2578
13	0.004098	0.221736	1.882947	903.8214	43.47028	10064.23	90.45553
14	0.003661	0.20165	1.848999	911.3979	40.44858	9918.768	98.84962
15	0.003345	0.189127	1.800468	934.112	38.34183	10058.48	109.5437
16	0.004441	0.245116	1.845013	926.4551	41.42825	11966.13	99.72737
17	0.004037	0.228253	1.800367	940.452	39.32386	11916.54	108.2628
18	0.003038	0.174078	1.775999	946.5685	35.71793	10070.79	120.7481
19	0.002839	0.162952	1.772808	951.5591	33.8997	9985.126	128.5695
20	0.013815	0.310038	4.663782	929.5959	41.9079	15012.99	99.25554

Sequence Number	T1 Degs F	T2 Degs F	T3 Degs F	T4 Degs F	T5 Degs F	Power Watts	MJ/Kg
1	1034.83	1034.19	967.11	876.37	576.41	4118.853	40.65839
2	769.6	767.16	707.16	633.11	403.28	6036.845	39.77439
3	1246.67	1248.71	1161.55	1044.75	660.05	6118.042	51.18324
4	1025.19	1021.7	936.77	830.73	511.38	8058.18	50.10359
5	1452.72	1454.55	1347.56	1207.51	740.73	8109.417	60.77431
6	1268.65	1266.92	1157.14	1023.51	605.44	10142.36	60.44936
7	1140.4	1132.49	1023.1	895.92	519.5	12035.04	60.01354
8	1688.46	1695.23	1563.51	1400.13	851.32	10135.61	70.29899
9	1045.45	1041.74	952.22	847.27	513.79	8064.509	50.15913
10	1537.2	1533.07	1394.61	1234.31	716.27	12001.45	70.01292
12	2036.14	2060.4	1933.78	1750.02	1064.13	10136.48	80.2578
13	2249.04	2249.06	2217.39	2028.11	1237.04	10064.23	90.45553
14	-84.81	-145.17	2249.06	2210.65	1365.91	9918.768	98.84962
15	32	1470.47	32	2249.06	32	10058.48	109.5437
16	1119.68	32	2249.06	2127.58	1204.18	11966.13	99.72737
17	1065.99	32	1048.18	2249.05	1357.65	11916.54	108.2628
18	628.92	32	32	99.26	1519.38	10070.79	120.7481
19	298.88	32	32	759.81	1613.46	9985.126	128.5695
20	2249.06	2249.06	2077.25	1890.76	1132.92	15012.99	99.25554

Sequence Number	T6 Degs F	T7 Degs F	T8 Degs F	T9 Degs F	T10 Degs F	Power Watts	MJ/Kg
1	473.9	95.07	99.69	100.35	63.44	4118.853	40.65839
2	329.33	97.38	96.62	97.24	65.26	6036.845	39.77439
3	540.17	110.24	111.41	111.81	65.69	6118.042	51.18324
4	412.64	106.37	104.26	104.94	66.74	8058.18	50.10359
5	602.22	114.24	114.61	115.08	67.28	8109.417	60.77431
6	483.51	91.66	91.63	92.67	66.33	10142.36	60.44936
7	404.67	95	92.32	92.97	68	12035.04	60.01354
8	674.39	119.52	114.85	115.31	68.64	10135.61	70.29899
9	411.8	113.66	109.53	110.4	69.26	8064.509	50.15913
10	565.63	94.92	93.52	94.15	64.98	12001.45	70.01292
12	846.57	138.54	134.52	135.11	66.87	10136.48	80.2578
13	992.64	152.47	148.46	148.37	66.49	10064.23	90.45553
14	1092.84	169.39	165.13	164.76	66.82	9918.768	98.84962
15	1178.81	183.36	179.54	178.6	67.59	10058.48	109.5437
16	1015.39	157.35	153.85	153.92	68.09	11966.13	99.72737
17	1107.13	178.02	170.24	170.1	69.21	11916.54	108.2628
18	1241.22	201.77	199.84	198.47	70.81	10070.79	120.7481
19	1288.34	208.17	204.46	202.28	71.12	9985.126	128.5695
20	877.77	161.51	139.03	139.86	66.81	15012.99	99.25554

Sequence Number	Fgas Lbf	Fgascorr Lbf	Farc Lbf	IspgasCor seconds	Flow Lbm/S	Power Watts	MJ/Kg
1	0.096728	0.10506	0.042565	470.3287	0.000223	4118.853	40.65839
2	0.135791	0.149783	0.069786	447.5561	0.000335	6036.845	39.77439
3	0.12277	0.133016	0.060078	504.6735	0.000264	6118.042	51.18324
4	0.171133	0.177434	0.081353	500.3348	0.000355	8058.18	50.10359
5	0.159972	0.165045	0.067478	560.9515	0.000294	8109.417	60.77431
6	0.186014	0.202233	0.092093	546.6342	0.00037	10142.36	60.44936
7	0.223217	0.231535	0.121581	523.6131	0.000442	12035.04	60.01354
8	0.176714	0.189639	0.078135	596.5121	0.000318	10135.61	70.29899
9	0.163693	0.178771	.0.083	504.268	0.000355	8064.509	50.15913
10	0.206476	0.223086	0.095938	590.2129	0.000378	12001.45	70.01292
12	0.163693	0.174352	0.06743	626.0639	0.000278	10136.48	80.2578
13	0.156252	0.16035	0.061386	653.6048	0.000245	10064.23	90.45553
14	0.145091	0.148752	0.052898	672.3135	0.000221	9918.768	98.84962
15	0.13393	0.137275	0.051851	678.0146	0.000202	10058.48	109.5437
16	0.178574	0.183014	0.062102	691.7311	0.000265	11966.13	99.72737
17	0.163693	0.167729	0.060523	691.0827	0.000243	11916.54	108.2628
18	0.12277	0.125807	0.048271	684.0904	0.000184	10070.79	120.7481
19	0.115329	0.118167	0.044785	690.0391	0.000171	9985.126	128.5695
20	0.212056	0.225872	0.084167	677.2371	0.000334	15012.99	99.25554

Cold Hydrogen Flow Data

Sequence Number	Flow Lbm/S	Fmeas Lbf	Fcorr Lbf	Pi Psi	Palt Mtorr	ISPcorr seconds	Tgas Degs F
CF1	0.000137	0.030016	0.034375	12.45478	123.9125	251.3155	66.04
CF2	8.95E-05	0.019808	0.022667	8.476154	81.26929	253.3065	63.39
CF3	0.000177	0.040562	0.04677	16.46217	176.4349	264.4208	62.68
CF4	8.9E-05	0.020209	0.020209	8.651001	80	227.1604	65.88
CF5	0.000134	0.030494	0.030494	12.53962	124	228.2307	65.31
CF6	0.000178	0.040826	0.047022	16.58821	176.1276	264.8895	65.15
CF7	8.49E-05	0.018509	0.021175	7.95513	75.78052	249.5331	60.54
CF8	0.000132	0.030035	0.034421	12.45212	124.6885	260.347	60.47
CF9	0.000177	0.041695	0.047971	16.73274	178.3991	270.6827	60.67
CF10	9.02E-05	0.019789	0.022717	7.793006	83.23537	251.851	56.79
CF11	0.00013	0.029336	0.033732	11.06992	124.9364	259.5874	56.3
CF12	0.000178	0.040672	0.047107	14.83578	182.8998	265.1826	56.45
CF13	9.02E-05	0.019955	0.019955	7.998506	80	221.1128	56.03
CF14	0.000132	0.02989	0.02989	11.43478	124	226.5493	55.51
CF15	0.000177	0.041063	0.041063	15.08565	176	231.7712	55.32